Robotica (2015) volume 33, pp. 1201–1230. © Cambridge University Press 2014
doi:10.1017/S026357471400023X

Dynamic model and input shaping control of a flexible link parallel manipulator considering the exact boundary conditions

Quan Zhang†,‡, James K. Mills‡*,
William L. Cleghorn‡, Jiamei Jin† and Zhijun Sun†

†*State Key Laboratory of Mechanics and Control of Mechanical Structures, Nanjing University of Aeronautics and Astronautics, Nanjing, P.R. China*
‡*Department of Mechanical and Industrial Engineering, University of Toronto, Toronto, Canada*

(Accepted January 30, 2014. First published online: April 1, 2014)

SUMMARY
In this paper, a rigid–flexible planar parallel manipulator (PPM) actuated by three linear ultrasonic motors for high-accuracy positioning is proposed. Based on the extended Hamilton's principle, a rigid–flexible dynamic model of the proposed PPM is developed utilizing exact boundary conditions. To derive an appropriate low-order dynamic model for the design of the controller, the assumed modes method is employed to discretize elastic motion. Then to investigate the interaction between the rigid and elastic motions, a proportional derivative feedback controller combined with a feed-forward-computed torque controller is developed to achieve motion tracking while attenuating the residual vibration. Then the controller is extended to incorporate an input shaper for the further suppression of residual vibration of flexible linkages. Computer simulations are presented as well as experimental results to verify the proposed dynamic model and controller. The input shaping method is verified to be effective in attenuating residual vibration in a highly coupled rigid–flexible PPM. The procedure employed for dynamic modeling and control analysis provides a valuable contribution into the vibration suppression of such a PPM.

KEYWORDS: Flexible parallel manipulator; Dynamic model; Exact boundary conditions; PD feedback; Input shaping.

1. Introduction

The demand for a precise positioning platform manipulator with a large workspace has increased dramatically due to its role in semiconductor manufacturing and automatic micro-assembly. Industrial manipulators according to their configuration are mainly classified as serial or parallel platforms. In general, serial platforms have the advantage of a large workspace and can achieve greater numbers of degrees of freedom (DOF) by stacking multiple stages. However, these stacked structures lead to the accumulation of positioning errors, and hence precise positioning is difficult to achieve. Compared with serial platform manipulators, parallel platform manipulators exhibit higher kinematic precision, better stiffness, and greater load bearing capacity.[1] Hence, parallel structure robots have been the focus of much research in the past decade.

With the development of lead zirconate titanate (PZT) ceramic-based actuators, many direct drive robotic platforms have been designed for high precision tasks. Linear ultrasonic motors (LUSM), as PZT material-based actuators, have the following characteristics: (a) direct actuation ability; (b) very high position accuracy, in the range of nanometers; (c) no error accumulation from transmission components; and (d) relatively simple to integrate with a variety of systems.[2] Hence, a novel butterfly-shaped LUSM,[3] as shown in Fig. 1, is chosen to actuate the proposed planar parallel manipulator (PPM).

* Corresponding author. E-mail: mills@mie.utoronto.ca

https://doi.org/10.1017/S026357471400023X Published online by Cambridge University Press

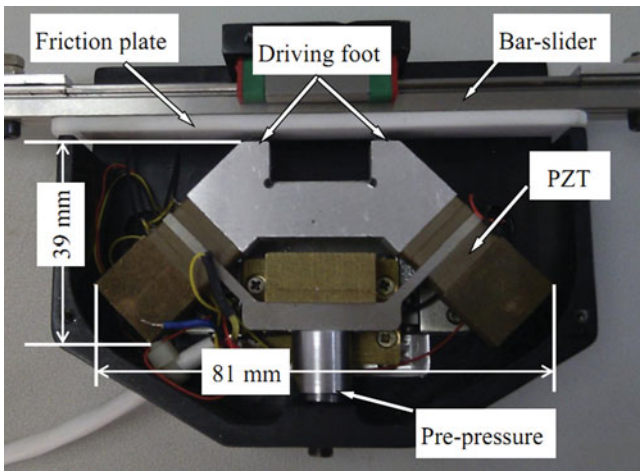


Fig. 1. Butterfly-shaped LUSM applied in the prototype.

Lightweight linkages are adopted to achieve high speed and acceleration. However, due to undesired deflections of these linkages, this leads to a motion tracking error of the manipulator, and may even cause system instability. To address these concerns, a rigid–flexible dynamic model must first be developed to examine both the dynamic features of these undesired deflections and the interaction influences between rigid and elastic motions. The rigid dynamic model is typically developed using the Newton–Euler algorithm and the Lagrangian formulation. The most common approaches used to discretize the flexible deformation is the Finite Element Method (FEM),[4,5] and the assumed modes method (AMM).[6–9] Early investigations have primarily focused on modeling of serial elastic link robot,[10–12] and a detailed review was provided by Dwivedy and Eberhard.[13] In contrast, little research literature on dynamic modeling for flexible robots with parallel structure has been published. Wang and Mills[14] presented an FEM model of a PPM with elastic linkages for active vibration analysis using a sub-structure methodology. Yu *et al.*[15] developed a dynamic model of a 3-RRR robot with elastic linkages, and experiments were carried out to verify the effectiveness of the model presented. Liu *et al.*[16] investigated a dynamic model of a 3-RRS flexible robot with a parallel structure based on a spatial element model of elastic links. Using AMM, Zhang *et al.*[17] presented a dynamic model of a PPM focused on the one-way modeling method. Hu *et al.*[18] conducted the experiments of active vibration control of a five-bar flexible PPM with PZT actuators and strain gauges. Sun *et al.*[19] investigated a high-speed parallel Delta-S manipulator based on kinetostatic analysis. However, to obtain an accurate dynamic model of a PPM for vibration analysis, exact boundary conditions, which accurately model the linkage dynamic behavior, must be considered. Due to the closed-chain structure of the PPM, it is usually problematic to determine the actual boundary conditions of flexible links. Hence, sub-structure analysis[14,20] is proposed to solve this problem.

Since structural deflection of the linkages will decrease the positioning accuracy of the end-effector, vibration control has received much interest from many researchers. Matsuno *et al.*[21] proposed a proportional derivative and strain (PDS) feedback controller to achieve vibration suppression of a space truss structure with a parallel structure. Using the deflection signal in the feedback, Mansour *et al.*[22] presented a modified proportional-integral-derivative (PID) control to track joint motions while attenuating the deflection of a flexible arm. A Linear Quadratic Regulator (LQR) incorporated a feed-forward input shaper and is studied by Ahmad and Mohamed.[23] However, these control approaches mainly focus on single or multiple flexible links of serial structure manipulators. Relatively little work has been published on the control of rigid–flexible PPMs. Liu and Sun[24] developed a proportional derivative (PD) feedback controller to regulate an elastic link simultaneously operated by two rigid arms to a desired position while attenuating its deflection. To achieve high precision motion of parallel manipulator, Su *et al.*[25] developed a saturated PD control law based on synchronized errors, with the experimental work conducted on a 3-DOF PPM, to establish the effectiveness of the established controller. Using a singular perturbation model, a hybrid controller, in which the controller for rigid and elastic motions is designed separately, was developed to control a flexible PPM.[26] The control methods discussed here are based on joint motion control, which have the advantage of simple

https://doi.org/10.1017/S026357471400023X Published online by Cambridge University Press

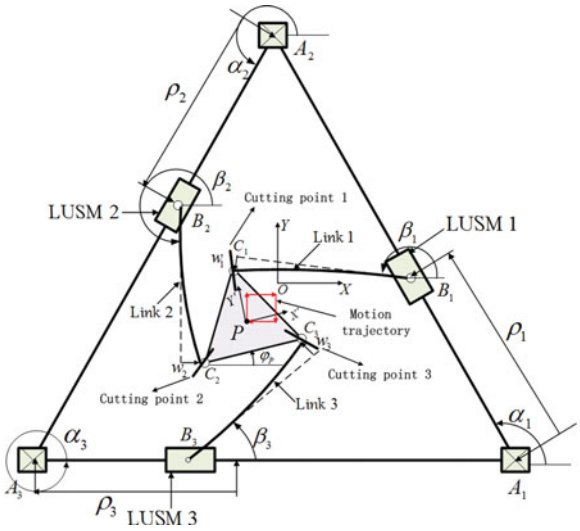


Fig. 2. Schematic model of a 3-PRR PPM.

implementation, compared with the active vibration control method using vibration sensors and actuators.

The input shaping control technique, a feed-forward approach, which has been developed for vibration attenuation, has been widely used in many flexible manipulators. The commonly used input shapers include zero-vibration (ZV) shaper, zero-vibration-derivative (ZVD) shaper, zero-vibration-derivative-derivative (ZVDD) shaper, and extra insensitive (EI) shaper. These input shapers have not only proved effective in conventional single or multiple flexible link serial manipulators,[27–29] but have been also validated and applied to nonlinear systems such as rigid–flexible parallel structure manipulators.[30,31] The main objective of the PPM controller is to achieve motion tracking of moving platforms while simultaneously suppressing the undesired vibration. Based on the above literature and dynamic model presented, a PD feedback control law combined with a feed-forward-computed torque is developed. The stability of the proposed controller is also investigated. Then the controller is extended to incorporate a ZVD input shaper for further attenuating the deflection of elastic linkages. Finally, experimental results are provided and compared with simulation results to verify the assumptions used in the modeling procedure and also validate the effectiveness of input shaper.

This paper is organized as follows. Section 2 presents the structure of the proposed PPM and its inverse dynamic analysis. The dynamic model is then formulated in Section 3. Section 4 provides the analysis of the proposed controller. Numerical simulations and experiments' results are given in Sections 5 and 6 respectively. Finally, concluding remarks are presented in Section 7.

2. Inverse Kinematic Analysis

Considering the beneficial features of parallel structure robots with lightweight linkages and previous research,[32,33] a 3-PRR-type PPM with lightweight links actuated with LUSMs is developed to achieve planar motion tracking and positioning, i.e. with coordinates $x - y - \varphi$. The PPM comprises a moving platform and three symmetric flexible linkages. Each prismatic joint is directly driven by an LUSM, which has an accuracy of 50 nm and thrust of 25 N. The reachable workspace is 60×60 mm with the rotation range of motion of 40°. A schematic of the prototype PPM is shown in Fig. 2, with the experimental PPM setup shown in Fig. 25.

The coordinate frames of the PPM are shown in Fig. 2. From the geometry of Fig. 2, the following closed-loop kinematic constraint equations must be satisfied due to the parallel structure of the PPM:

$$x_p + x'_{ci}\cos\varphi_p - y'_{ci}\sin\varphi_p = x_{Ai} + \rho_i\cos\alpha_i + L_i\cos\beta_i - w_i(L)\sin\beta_i, \quad i = 1, 2, 3, \tag{1}$$

$$y_p + x'_{ci}\sin\varphi_p + y'_{ci}\cos\varphi_p = y_{Ai} + \rho_i\sin\alpha_i + L_i\sin\beta_i + w_i(L)\cos\beta_i, \quad i = 1, 2, 3, \tag{2}$$

https://doi.org/10.1017/S026357471400023X Published online by Cambridge University Press

where x_{Ai} and y_{Ai} are the coordinates of point A_i, x'_{ci} and y'_{ci} are the positions of C_i in a moving frame, and L_i is the length of the linkage. The prismatic motion of the LUSM is defined as ρ_i $(i = 1, 2, 3)$. The initial position of ρ_i is chosen at the location at which the moving coordinate frame $X'PY'$ is coincident with static coordinate frame XOY. The coordinates of the moving platform are represented as a vector of $\overline{X}_p = (x_p, y_p, \varphi_p)^T$ in the static coordinate system, and $w_i(L)$ is the flexible deformation at the tip of the ith linkage.

Combining Eqs. (1) to (2) and eliminating β_i, we obtain

$$\rho_i^2 - Q_{i1}\rho_i + Q_{i2} = 0, \tag{3}$$

$$\rho_i = \frac{Q_{i1} \pm \sqrt{Q_{i1}^2 - 4Q_{i2}}}{2}, \tag{4}$$

where

$$Q_{i1} = 2\cos\alpha_i Q_{i3} + 2\sin\alpha_i Q_{i4}; \quad Q_{i2} = Q_{i3}^2 + Q_{i4}^2 - L_i^2 - w_i(L)^2,$$
$$Q_{i3} = x_p - x_{Ai} + x'_{ci}\cos\varphi_p - y'_{ci}\sin\varphi_p,$$
$$Q_{i4} = y_p - y_{Ai} + x'_{ci}\sin\varphi_p + y'_{ci}\cos\varphi_p.$$

Equation (4) shows that for a given configuration of the moving platform, the position of each LUSM has two possible solutions. Hence, the solution of ρ_i must be selected based on the desired trajectory and initial configuration of a moving platform.

3. Dynamic Modeling

3.1. Dynamic model of ith *individual flexible link*

In the following, we adopt the substructure approach to model the dynamic equations of the PPM.[14,20] The PPM is first divided into several symmetrical parts, and then the extended Hamilton's algorithm is employed to determine both the exact boundary conditions and the equations of motion. Finally, the complete model is obtained by eliminating constraint forces. Compared with passive joint B_i, which moves along the linear guide rail, passive joint C_i has three DOFs in the xy plane. Therefore, it is reasonable to consider the proximal end of the flexible link to be pinned at point B_i, while the distal end of the link to be free, but modeled with constraint forces at point C_i. Thus, the PPM is divided into three symmetric branches and one moving platform at point C_i, as shown in Fig. 2. This assumption is also validated through the modal test experiments provided in Section 6.1. Due to the symmetrical structure of the PPM, only one of the three branches is chosen to develop the equations of motions.

As illustrated in Fig. 3, the deflection of the linkage is sufficiently small with respect to the length of the linkage, and therefore the Euler–Bernoulli beam theory is adopted to model the flexible behavior of the linkage. The geometrical details of the links are illustrated in Section 6.1. The effect of axial forces is also considered in this model. Since the platform moves in the horizontal plane, forces due to gravity are ignored. Parameters f_{ia} and f_{iv} are the constraint forces applied by the passive joint C_i.

The total kinetic energy of the ith branch is presented as[34]

$$T_i = T_{Li} + T_{Bi} + T_{Si}, \tag{5}$$

where $T_{Li} = \frac{1}{2}\int_0^{L_i} \rho_{Ai}\dot{\bar{r}}_i^2 dx$, the kinetic energy of the ith flexible link,

$T_{Bi} = \frac{1}{2}m_{Bi}\dot{\bar{r}}_{Bi}^2 + \frac{1}{2}J_{Bi}(\dot{\beta}_i + \dot{w}'_{Bi})^2$, the kinetic energy of joint B_i,
$T_{Si} = \frac{1}{2}m_{Si}\dot{\rho}_i^2$, the kinetic energy of the ith slider,
$\bar{r}_i = [x_{Ai} + \rho_i\cos\alpha_i + x\cos\beta_i - w_i(x,t)\sin\beta_i]i + [y_{Ai} + \rho_i\sin\alpha_i + x\sin\beta_i + w_i(x,t)\cos\beta_i]j$, the position vector $\bar{r}_i$, and
w_i is the transverse elastic displacement.

https://doi.org/10.1017/S026357471400023X Published online by Cambridge University Press

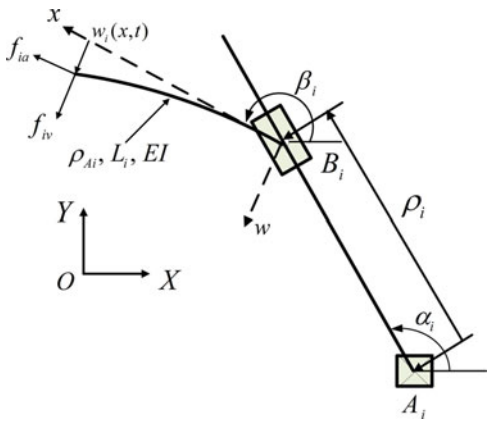


Fig. 3. Schematic model of the ith branch.

The potential energy of the ith branch is expressed as

$$V_i = \frac{1}{2}\int_0^{Li} EI(w_i'')^2 dx + \frac{1}{2}\int_0^{Li} P_{xi}(w_i')^2 dx, \tag{6}$$

where E is Young's modulus of elasticity, and $P_{xi} = (m_{si} - F_{ai})C_i + \rho_{Ai}(\ddot{\rho}_i C_i x - \frac{1}{2}\dot{\beta}_i^2 x^2) + f_{ia}$ is the axial forces.[35] The first term in Eq. (6) is the strain energy of the elastic linkage, while the second term is the work done by axial forces.

The virtual work of the non-conservative force of the branch can be written as

$$\delta \bar{W}_{nc} = \bar{f}_{ixy} \cdot \delta \bar{r}_{Ci} + F_{ai}\delta\rho_i, \tag{7}$$

where $\delta\bar{r}_{ci}$ represents the virtual displacement at the tip of the linkage, and $\bar{f}_{ixy} = \left[\begin{smallmatrix}\cos\beta_i & -\sin\beta_i \\ \sin\beta_i & \cos\beta_i\end{smallmatrix}\right]\left[\begin{smallmatrix} f_{ia} \\ f_{iv}\end{smallmatrix}\right]$ is the constraint force transferred to the static frame direction.

The differential equations and the boundary-value problem of the branches are developed utilizing the extended Hamilton's principle, which is presented as[8]

$$\int_{t_1}^{t_2} (\delta T - \delta V + \delta \bar{W}_{nc})dt = 0. \tag{8}$$

Evaluating the variation of Eqs. (5) and (6), and substituting the result into Eq. (8), and integrating by parts, leads to the associated boundary-value expressed as

$$\begin{aligned} &w_i(0,t) = 0, && E_i I_i w_i''(0,t) = J_{Bi}[\ddot{\beta}_i + \ddot{w}_i'(0,t)], \\ &E_i I_i w_i''(L_i,t) = 0, && E_i I_i w_i'''(L_i,t) = -f_{iv} + P_{xi} w_{ci}'. \end{aligned} \tag{9}$$

The non-homogeneous boundary conditions can be transformed into differential equations by means of a Dirac function defined as $\delta(x_i - L_i) = 0, x \neq L_i$, and $\int_0^{L_i} \delta(x_i - L_i)dx_i = 1$.[8] In view

https://doi.org/10.1017/S026357471400023X Published online by Cambridge University Press

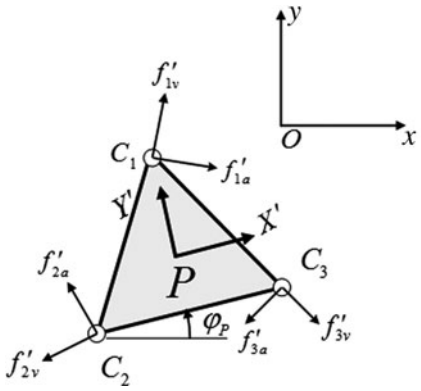


Fig. 4. Coordinates system of the moving platform.

of this, the equation of motion and the associated boundary values can be written as[34]

$$F_{ai} + C_i f_{ia} + S_i f_{iv} = (m_{Si} + m_{Bi})\ddot{\rho}_i + \int_0^{L_i} \rho_{Ai}[(\ddot{\rho}_i - 2C_i\dot{\beta}_i\dot{w}_i - C_i w_i\ddot{\beta}_i - S_i w_i\dot{\beta}_i^2 + S_i\ddot{w}_i + xS_i\ddot{\beta}_i - xC_i\dot{\beta}_i^2)dx, \tag{10}$$

$$-w_{Ci} f_{ia} + L_i f_{iv} = \int_0^{L_i} \rho_{Ai}(x^2\ddot{\beta}_i + x\ddot{w}_i - C_i w_i\ddot{\rho}_i + xS_i\ddot{\rho}_i)dx + J_{Bi}(\ddot{\beta}_i + \ddot{w}'_{Bi}), \tag{11}$$

$$\rho_{Ai}(\ddot{w}_i + x\ddot{\beta}_i + S_i\ddot{\rho}_i - w_i\dot{\beta}_i^2) + E_i I_i w'''' - P_{xi} w''_i - P'_{xi} w'_i = (f_{iv} - P_{xi} w'_i)\delta(x_i - L_i) + J_{Bi}[\ddot{\beta}_i + \ddot{w}'_i]\delta'(x_i), \tag{12}$$

with homogeneous boundary conditions

$$\begin{aligned} &w_i(0,t) = 0, && E_i I_i w''_i(0,t) = 0, \\ &E_i I_i w''_i(L_i,t) = 0, && E_i I_i w'''_i(L_i,t) = 0. \end{aligned} \tag{13}$$

From Eqs. (12) and (13), it is shown that the constraint forces at the ends of flexible linkages are transformed to elastic motion, and hence an accurate rigid–flexible model with exact boundary conditions is obtained.

3.2. Equations of moving platform

The triangular-shaped moving platform is assumed to be rigid. The forces exerted on the moving platform are the reaction forces provided by passive joint, which has the relations $\bar{f}'_{ixy} = -\bar{f}_{ixy}$, as shown in Fig. 4.

The equation of motion is obtained by means of Newton's Second Law[34]

$$M_P\ddot{\bar{X}}_P = [\,M_{P1} \quad M_{P2} \quad M_{P3}\,]\begin{bmatrix} \bar{f}_1 \\ \bar{f}_2 \\ \bar{f}_3 \end{bmatrix} + F_f, \tag{14}$$

where $\bar{f}_i = \begin{pmatrix} f_{ia} & f_{iv} \end{pmatrix}^T$, F_f is the friction force, with other terms detailed in Appendix A.

3.3. Discrete equation of elastic motions

Equations (10)–(12) constitute a highly nonlinear, coupled set of differential equations between rigid and elastic motions. An analytical solution cannot be found, and approximate numerical method must be used for simulation. Here AMM is chosen to discrete the equations of elastic motion.

https://doi.org/10.1017/S026357471400023X Published online by Cambridge University Press

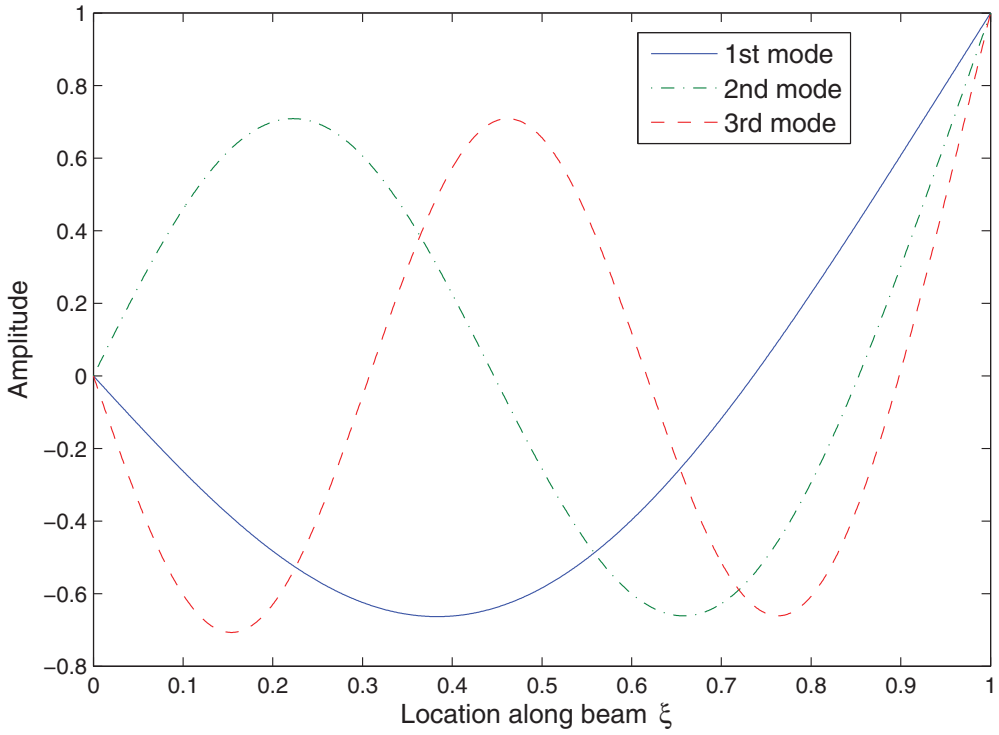


Fig. 5. Amplitude of the first three mode shapes.

We assume

$$w_i(x,t) = \sum_{j=1}^{r} Y_{ij}(x) q_{ij}(t) \quad i = 1, 2, 3, \tag{15}$$

where $q_{ij}(t)$ represents the unknown generalized coordinates of ith linkage, and $Y_{ij}(x)$ is chosen as normalized shape functions matching pinned-free boundary conditions,[8]

$$Y_{ij}(x) = \frac{1}{\sqrt{m_i L_i}\sin\theta_j}\left[\sin\left(\frac{\theta_j x_i}{L_i}\right) + \frac{\sin\theta_j}{\sinh\theta_j}\sinh\left(\frac{\theta_j x_i}{L_i}\right)\right] \tag{16}$$

where $\theta_j = (j + 0.25)\pi$, $j = 1, 2, \ldots, r$ and $0 \le x_i \le L_i$.

Figure 5 illustrates the shape functions of the first three modes, where $0 \le \xi = x/L \le 1$ represents the location along beam.

Substituting Eqs. (15) and (16) into Eqs. (10)–(12), algebraic manipulation yields the following nonlinear coupled dynamic equations:

$$M(\bar{\eta})\ddot{\bar{\eta}} + N(\bar{\eta}, \dot{\bar{\eta}}) + K\bar{\eta} = \bar{u}(t) + A(\bar{\eta})\bar{f}_{in}, \tag{17}$$

where $\bar{\eta}$ represents the generalized coordinates of the PPM, including both rigid and elastic motions, $M(\bar{\eta})$ represents the configuration-dependent mass matrix, $N(\bar{\eta}, \dot{\bar{\eta}})$ represents the Coriolis and centrifugal terms, K is the stiffness matrix, and $\bar{u}(t)$ represents the actuation force. The last term represents the internal constraint force applied on the end of the beam. Equation (17) is given below

https://doi.org/10.1017/S026357471400023X Published online by Cambridge University Press

in detail with $9 + 3r$ equations,

$$\begin{bmatrix} M_{11} & M_{12} & 0 & M_{14} \\ M_{12}^T & M_{22} & 0 & M_{24} \\ 0 & 0 & M_{33} & 0 \\ M_{14}^T & M_{24}^T & 0 & M_{44} \end{bmatrix} \begin{bmatrix} \ddot{\bar{\rho}} \\ \ddot{\bar{\beta}} \\ \ddot{\bar{X}}_P \\ \ddot{\bar{q}} \end{bmatrix} + \begin{bmatrix} N_1 \\ 0 \\ -F_f \\ N_4 \end{bmatrix} + \begin{bmatrix} 0 & 0 & 0 & 0 \\ 0 & 0 & 0 & 0 \\ 0 & 0 & 0 & 0 \\ 0 & 0 & 0 & K_f \end{bmatrix} \begin{bmatrix} \bar{\rho} \\ \bar{\beta} \\ \bar{X}_P \\ \bar{q} \end{bmatrix}$$
$$= \begin{bmatrix} F_a \\ 0 \\ 0 \\ 0 \end{bmatrix} + \begin{bmatrix} M_{\rho 1} & M_{\rho 2} & M_{\rho 3} \\ M_{\beta 1} & M_{\beta 2} & M_{\beta 3} \\ M_{P1} & M_{P2} & M_{P3} \\ M_{W1} & M_{W2} & M_{W3} \end{bmatrix} \begin{bmatrix} \bar{f}_1 \\ \bar{f}_2 \\ \bar{f}_3 \end{bmatrix}, \tag{18}$$

where $\bar{f}_i = [f_{ia}\ f_{iv}]^T$, $\bar{\rho} = [\rho_1\ \rho_2\ \rho_3]^T$, $\bar{\beta} = [\beta_1\ \beta_2\ \beta_3]^T$, $\bar{q} = [q_{11}\ \cdots\ q_{1r}\ q_{21}\ \cdots\ q_{2r}\ q_{31}\ \cdots\ q_{3r}]^T \in R^{3r\times 1}$, and other items are detailed in Appendix A.

4. Control Schemes

4.1. PD feedback control

Since the constraint forces $\bar{f}_i$ are internal to the overall system in Eq. (18), the equations of motion are not in a form suitable for controller synthesis. Hence, Eq. (18) must be transformed to an appropriate form for controller design. As shown in Fig. 2, certain geometric constraints hold due to the closed-chain structure of the PPM. Differentiating the constraint Eqs. (1) and (2) twice with respect to time, with algebraic manipulation yields,

$$\ddot{\bar{X}}_p = \begin{bmatrix} J_P' & \bar{0}_{3\times 3r} \end{bmatrix} \begin{bmatrix} \ddot{\bar{\rho}} \\ \ddot{\bar{q}} \end{bmatrix} + \begin{bmatrix} \dot{J}_P' & J_P' J_{PW} \end{bmatrix} \begin{bmatrix} \dot{\bar{\rho}} \\ \dot{\bar{q}} \end{bmatrix}, \tag{19}$$

$$\ddot{\bar{\beta}} = \begin{bmatrix} J_\beta' & J_{\beta W} \end{bmatrix} \begin{bmatrix} \ddot{\bar{\rho}} \\ \ddot{\bar{q}} \end{bmatrix} + \begin{bmatrix} \dot{J}_\beta' & \bar{0}_{3\times 3r} \end{bmatrix} \begin{bmatrix} \dot{\bar{\rho}} \\ \dot{\bar{q}} \end{bmatrix}, \tag{20}$$

where $J_P' = J_p^{-1}$, $J_\beta' = J_\beta J_p^{-1}$, J_P, J_β, J_{PW}, and $J_{\beta W}$ are Jacobian matrices from variables $\bar{\beta}$ and $\bar{\rho}$ to the end-effecter coordinates $\bar{X}_p$ and elastic motion $\bar{q}$ respectively. The matrix $\bar{0}_{3\times 3r}$ is the result of neglecting the higher order terms of w_i and $\dot{w}_i$.

To facilitate the controller design, Eq. (18) must be reduced to $3 + 3r$ equations with the constraint forces f_i removed. $\bar{\rho}$ and $\bar{q}$ are chosen as the independent coordinates of the PPM. Partitioning Eq. (18) in appropriate form and considering Eqs. (19) and (20) gives

$$M_S \begin{bmatrix} \ddot{\bar{\rho}} \\ \ddot{\bar{q}} \end{bmatrix} + H_S(\dot{\bar{\rho}}, \dot{\bar{q}}) + \begin{bmatrix} 0 & 0 \\ 0 & K_f \end{bmatrix} \begin{bmatrix} \bar{\rho} \\ \bar{q} \end{bmatrix} = \begin{bmatrix} F_a \\ 0 \end{bmatrix}, \tag{21}$$

where

$$H_S = \left(\begin{bmatrix} M_{11} & M_{12} & 0 & M_{14} \\ M_{14}^T & M_{24}^T & 0 & M_{44} \end{bmatrix} - \begin{bmatrix} J_{f\rho}^T \\ J_{fw}^T \end{bmatrix} \begin{bmatrix} J_{f\beta}^T \\ J_{fp}^T \end{bmatrix}^{-1} \begin{bmatrix} M_{12}^T & M_{22} & 0 & M_{24} \\ 0 & 0 & M_{33} & 0 \end{bmatrix} \right) \begin{bmatrix} 0 & 0 \\ \dot{J}_\beta' & 0 \\ \dot{J}_P' & J_P' J_{PW} \\ 0 & 0 \end{bmatrix} \begin{bmatrix} \dot{\bar{\rho}} \\ \dot{\bar{q}} \end{bmatrix}$$
$$+ \begin{bmatrix} N_1 \\ N_4 \end{bmatrix} + \begin{bmatrix} J_{f\rho}^T \\ J_{fw}^T \end{bmatrix} \begin{bmatrix} J_{f\beta}^T \\ J_{fp}^T \end{bmatrix}^{-1} \begin{bmatrix} 0 \\ F_f \end{bmatrix}, \tag{22}$$

https://doi.org/10.1017/S026357471400023X Published online by Cambridge University Press

$$M_S = \left(\begin{bmatrix} M_{11} & M_{12} & 0 & M_{14} \\ M_{14}^T & M_{24}^T & 0 & M_{44} \end{bmatrix} - \begin{bmatrix} J_{f\rho}^T \\ J_{fw}^T \end{bmatrix} \begin{bmatrix} J_{f\beta}^T \\ J_{fp}^T \end{bmatrix}^{-1} \begin{bmatrix} M_{12}^T & M_{22} & 0 & M_{24} \\ 0 & 0 & M_{33} & 0 \end{bmatrix} \right) \begin{bmatrix} I_1 & 0 \\ J'_\beta & J_{\beta w} \\ J'_P & 0 \\ 0 & I_2 \end{bmatrix}. \tag{23}$$

Compared with the Kineto-Elasto-Dynamics (KED) assumption, which does not consider the influences of elastic motion on rigid body, Eq. (21) represents the interaction between rigid and elastic motions while considering the exact boundary conditions. The coupling factors appear in matrices M_S as well as H_S. Thus, the elastic vibration will decrease the tracking accuracy of the moving platform through coupling factors.

For further investigation of the controller and closed-loop stability, Eq. (21) can also be defined as follows:

$$\begin{bmatrix} M_{rr} & M_{fr} \\ M_{rf} & M_{ff} \end{bmatrix} \begin{bmatrix} \ddot{\bar{\rho}} \\ \ddot{\bar{q}} \end{bmatrix} + \begin{bmatrix} C_{rr} & C_{fr} \\ C_{rf} & C_{ff} \end{bmatrix} \begin{bmatrix} \dot{\bar{\rho}} \\ \dot{\bar{q}} \end{bmatrix} + \begin{bmatrix} 0 \\ K_f \bar{q} \end{bmatrix} = \begin{bmatrix} F_a \\ 0 \end{bmatrix}, \tag{24}$$

where the subscripts r and f are used to denote the rigid and elastic coordinates respectively.

The principle utilized for controller design is that the moving platform must achieve motion tracking while the residual vibrations are simultaneously attenuated. To achieve this, a PD controller combined with a feed-forward-computed torque controller is developed. The advantage of this controller is that it is readily applicable and only requires the measurement of displacement and velocity of LUSMs. These measurements can be easily obtained by linear grating sensors mounted on LUSMs. The following gives the details of the control law[28]:

$$F_a = M_{rr} \ddot{\bar{\rho}}_d + C_{rr} \dot{\bar{\rho}}_d - K_p(\bar{\rho} - \bar{\rho}_d) - K_d(\dot{\bar{\rho}} - \dot{\bar{\rho}}_d), \tag{25}$$

where K_p and K_d are diagonal positive control gain matrices.

Since the elastic motion implemented on the moving platform is sufficiently small compared with the rigid motion, the elastic motion, i.e. $M_{fr}\ddot{\bar{q}} + C_{fr}\dot{\bar{q}}$ in Eq. (24) can be considered as a state-dependent disturbance. Hence, the PD with feed-forward-computed torque controller is able to achieve motion tracking. The following section demonstrates the stability analysis of the proposed controller.

At first, consider the Lyapunov candidate,

$$V = \frac{1}{2}\dot{\bar{\eta}}^T M_S \dot{\bar{\eta}} + \frac{1}{2}\bar{q}^T K_f \bar{q} + \frac{1}{2}\bar{e}^T K_p \bar{e} \geq 0, \tag{26}$$

where $\bar{e} = \bar{\rho} - \bar{\rho}_d$. Then differentiating V with respect to time gives

$$\dot{V} = \dot{\bar{\eta}}^T \left(M_s \ddot{\bar{\eta}} + \frac{1}{2}\dot{M}_s \dot{\bar{\eta}} \right) + \dot{\bar{q}}^T K_f \bar{q} + \dot{\bar{e}}^T K_p \bar{e}. \tag{27}$$

Substituting Eqs. (24) and (25) into Eq. (27), noting that when $t \geq T$, $\dot{\bar{\rho}}_d \equiv 0$, $\ddot{\bar{\rho}}_d \equiv 0$, $\dot{\bar{e}} = \dot{\bar{\rho}} - \dot{\bar{\rho}}_d = \dot{\bar{\rho}}$, and $\dot{M}_s - 2C$ is a skew-symmetric matrix after neglecting some centrifugal stiffening terms[12] lead to

$$\dot{V} = -\dot{\bar{\rho}}^T K_d \dot{\bar{\rho}} \leq 0. \tag{28}$$

Applying the LaSalle invariant set theory,[36] the asymptotically stability of the closed-loop dynamic of the PPM is proved, namely $\bar{\rho} \to \bar{\rho}_d$ and $\dot{\bar{\rho}},\ \bar{q},\ \dot{\bar{q}} \to 0$ as $t \to \infty$. Hence, the PD with feed-forward-computed torque controller can achieve simultaneous motion tracking while suppressing the residual vibration.

4.2. Input shaping with PD feedback control

To further suppress the vibration of a flexible linkage, an input shaper is developed to integrate the PD feedback controller designed above. An input shaper for vibration attenuation is usually

https://doi.org/10.1017/S026357471400023X Published online by Cambridge University Press

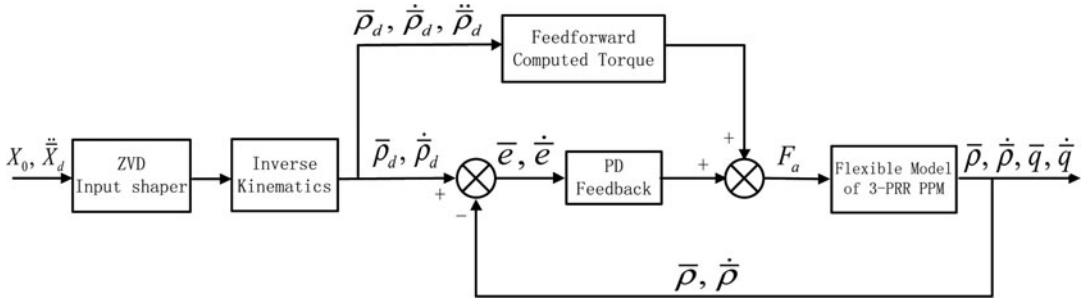


Fig. 6. The diagram of PD feedback with input shaping control.

designed using the inherent vibration nature of the robot. Although previous experimental studies with serial structure manipulator have proved that the input shaper achieved better results in vibration attenuation,[31,37] application of this approach to flexible parallel structures still presents a challenge. Hence, a PD feedback control integrated with an input shaper is proposed to track the desired trajectory of the moving platform while suppressing the undesired vibration of the flexible linkage, as shown in Fig. 6.

Based on the input shaper techniques,[30] a given motion is usually convolved with a series of impulse first, and then the resulting signal is decomposed. This signal is then used as an input to the system, applied at a time determined by minimizing the residual vibration after the last impulse ended. Hence, the key problems are to calculate the magnitude and time of the impulse based on the physical and vibration properties of the robot. Compared with ZV input shaper, the ZVD shaper exhibits strong robustness to parameter variation. If the vibration of the manipulator is given as[27]:

$$U(\omega, \varsigma) = e^{-\varsigma\omega t_n} \left\{ \sum_{i=1}^{n} [A_i e^{-\varsigma\omega(t-t_i)} \cos(\omega\sqrt{1-\varsigma^2} t_i)]^2 + \sum_{i=1}^{n} [A_i e^{-\varsigma\omega(t-t_i)} \sin(\omega\sqrt{1-\varsigma^2} t_i)]^2 \right\}^{\frac{1}{2}}, \tag{29}$$

then the following constraint equations of a ZVD input shaper must be satisfied:

$$U(\omega, \varsigma) = 0 \quad \sum_{i=1}^{n} A_i = 1 \quad \frac{\partial U(\omega, \varsigma)}{\partial \omega} = 0, \tag{30}$$

where ω represents the natural frequency, and ς represents the damping ratio.

The first constraint condition in Eq. (30) guarantees the vibration amplitude to be zero, and the second constraint condition means that the series of impulse need to be normalized. The third condition in Eq. (30) is used to ensure that the variation of the vibration also approaches zero. The amplitudes and time locations of a three-impulse ZVD shaper is calculated from Eq. (30) as

$$\begin{gathered} t_1 = 0 \quad t_2 = \frac{\pi}{\omega\sqrt{1-\varsigma^2}} \quad t_3 = \frac{2\pi}{\omega\sqrt{1-\varsigma^2}} \quad k = e^{\frac{-\varsigma\pi}{\sqrt{1-\varsigma^2}}} \\ A_1 = \frac{1}{1+2k+k^2} \quad A_2 = \frac{2k}{1+2k+k^2} \quad A_3 = \frac{k^2}{1+2k+k^2}. \end{gathered} \tag{31}$$

5. Simulation Results

Numerical simulations for the 3-PRR PPM are performed using the proposed control method. Two different comparison simulations are designed to investigate both the effectiveness of the rigid–flexible model and the proposed controller. During the simulation, a square trajectory motion of the

https://doi.org/10.1017/S026357471400023X Published online by Cambridge University Press

Table I. Calibrated kinematic parameters of the PPM.

Parameters	Ideal value	Calibrated value	Parameters	Ideal value	Calibrated value
α_1 (deg)	120	120.11	y'_{c1} (mm)	–34.64	–34.76
α_2 (deg)	240	238.56	y'_{c2} (mm)	69.28	70.32
α_3 (deg)	0	0.98	y'_{c3} (mm)	–34.64	–34.01
L_1 (mm)	200	201.51	x_{A1} (mm)	300	299.58
L_2 (mm)	200	200.67	x_{A2} (mm)	0	0.21
L_3 (mm)	200	199.89	x_{A3} (mm)	–300	–300.21
x'_{c1} (mm)	60	59.72	y_{A1} (mm)	–173.20	–172.63
x'_{c2} (mm)	0	0.31	y_{A2} (mm)	346.41	345.85
x'_{c3} (mm)	–60	–60.34	y_{A3} (mm)	–173.20	–174.22

moving platform is selected, as illustrated in Fig. 2. The moving platform is designed to perform four point-to-point motions with smooth acceleration and deceleration for each period. Taking the first period motion as an example gives

$$y_p(t) = \frac{y_f}{t_f}t - \frac{y_f}{2\pi}\sin\left(\frac{2\pi t}{t_f}\right),\ x_p = 0,\ \varphi_p = \frac{\pi}{6}, \tag{32}$$

where $y_f = 0.002$ m, $t_f = 0.03$ s. The elastic modulus is $E = 7.1 \times 10^{10}$ N/m^2 and other kinematic parameters used in the simulation are detailed in Table I in Section 6.2.

The first two vibration modes are chosen to model the elastic motion of the linkage. The positive diagonal gain matrices of a PD control are selected as $K_p = 3000\,I$, and $K_d = 600\,I$, where I is a 3×3 unit diagonal matrix. Considering the initial value of elastic coordinates $\bar{q} = \bar{0}_{9\times1}$ and $\dot{\bar{q}} = \bar{0}_{9\times1}$, and the initial values of $\bar{\rho}^d$ and initial velocity $\dot{\bar{\rho}}^d$ of LUSMs, Eq. (24) is simulated in MATLAB/Simulink software.

Figures 7 to 13 are based on these simulations, which show comparison of the dynamic behavior of the rigid model and the rigid–flexible model, both of which are controlled with PD feedback, in conjunction with the feed-forward-computed torque control law. The aim of the first comparison simulation is to validate the proposed rigid–flexible model and to study the interaction between rigid dynamics and elastic dynamics. The rigid model can be derived from Eq. (18) while ignoring the effect of elastic motions, i.e. $\bar{q}, \dot{\bar{q}}, \ddot{\bar{q}} \equiv 0$. The simulation results shown in Figs. 7 and 8 are tracking error profiles of the platform. These results reveal that even though the amplitude of the vibration computed through the flexible model decreases continuously, the approach still leads to persistently large oscillation of the moving platform. The angular position and angular acceleration are given in Figs. 9 and 10 respectively, which further validate the interaction between elastic and rigid motions. Due to the PD feedback with feed-forward-computed torque control, the orientation of the moving platform has not shown obvious oscillation. However, the acceleration of the moving platform exhibits obvious changes, which will further affect the dynamic characteristic of the PPM. Figures 11 and 12 illustrate the actuation forces provided by the three LUSMs and the constraint forces applied at the end of the first links respectively.

Figure 13 shows the error of the length of the location triangle on the moving platform in the rigid–flexible model, i.e. the error among points C_i. The error equation of C_1C_2 is expressed as $\Delta C_1C_2 = |\bar{r}_1(L_1, t) - \bar{r}_2(L_2, t)| - C_1C_2$. The simulation results have revealed that the constraint conditions are maintained during simulations, and hence the correct simulation of the parallel structure of the manipulator is carried out. However, geometric conditions are not strictly satisfied because the higher orders of elastic motion were neglected when developing the dynamic model.

Figures 14 to 18 are obtained based on the second comparison simulation, which is used to study the input shaping method in a highly coupled nonlinear system. The PD controller and the PD with input shaping controller are simulated in the rigid–flexible model. Here PD controller implies a PD feedback control plus a feed-forward-computed torque control. The first two modes are taken into consideration when calculating the impulse of a ZVD input shaper. From Eq. (18), the jth mode frequency of the ith elastic linkage is expressed as $\omega_{ij} = (EI\int_0^{Li} Y''_{ij}(x)dx/(\int_0^{Li} \rho_{Ai}Y^2_{ij}(x)dx + J_{Bi}Y^2_{ij}(0)))^{\frac{1}{2}}$, and the first two natural frequencies are calculated as $\omega_1 = 79.5$ Hz and $\omega_2 = 253.1$ Hz. The damping ratios are

https://doi.org/10.1017/S026357471400023X Published online by Cambridge University Press

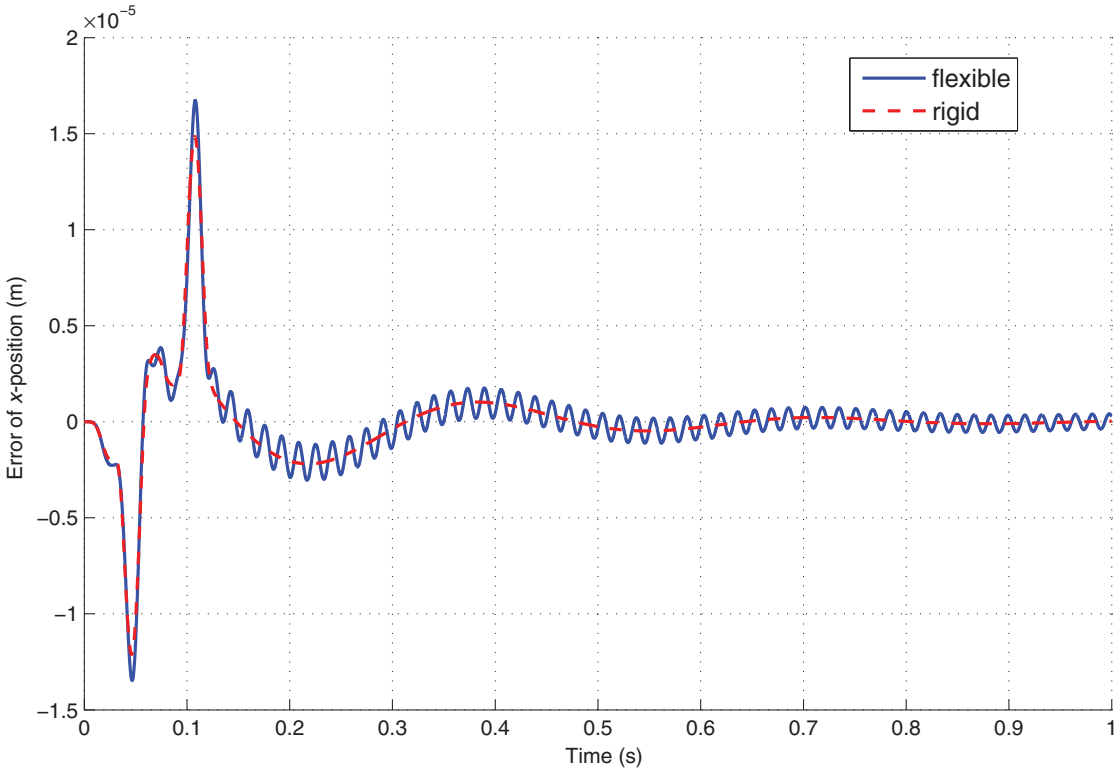


Fig. 7. Tacking error of the moving platform along x-axis.

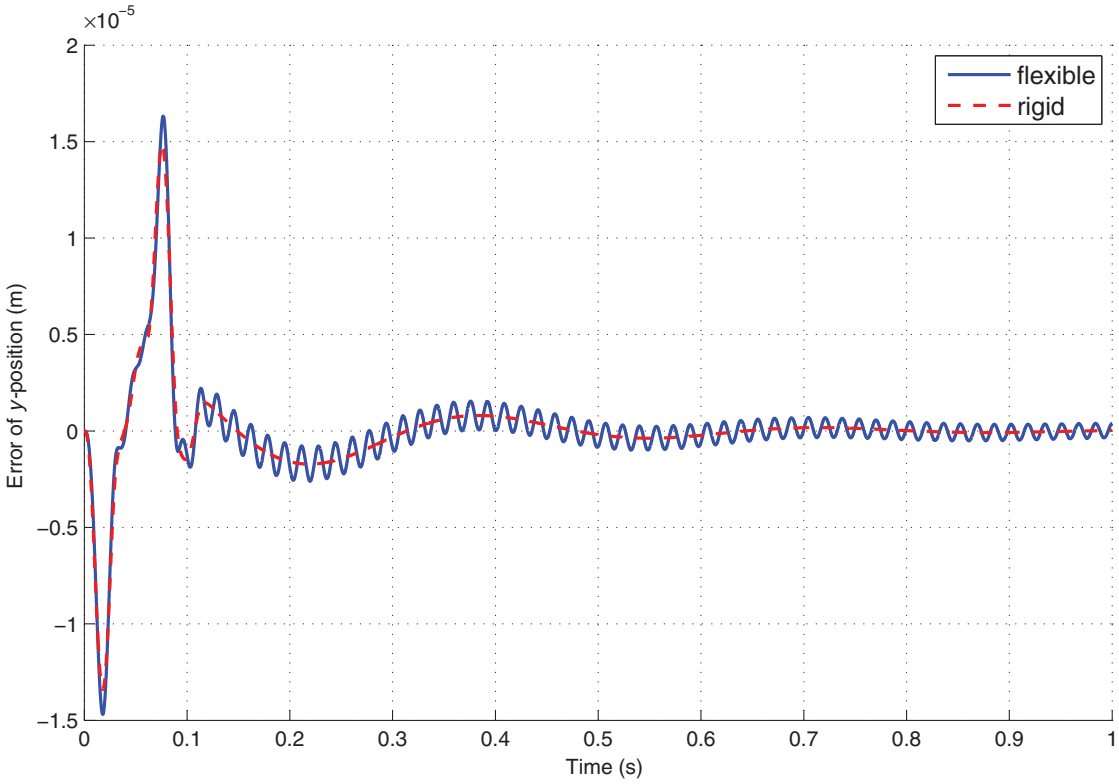


Fig. 8. Tracking error of the moving platform along y-axis.

https://doi.org/10.1017/S026357471400023X Published online by Cambridge University Press

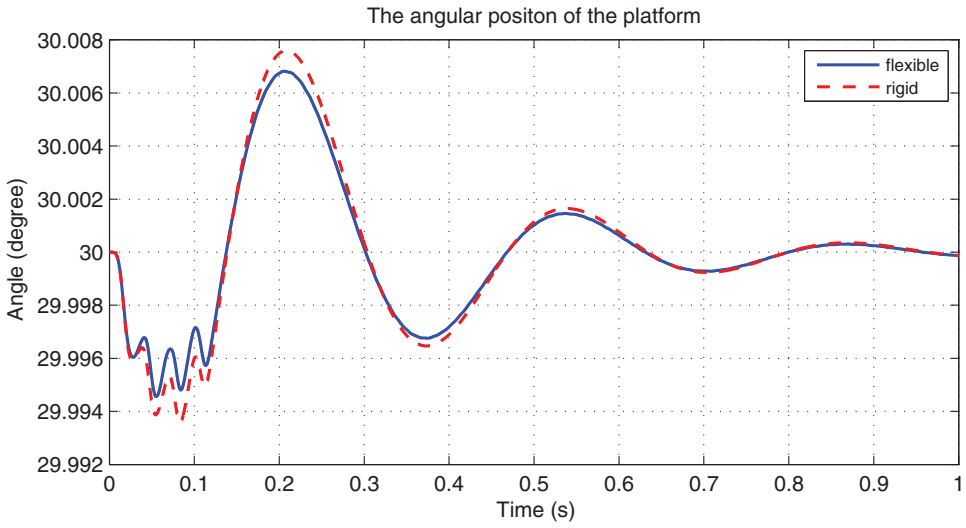


Fig. 9. Angular position of the moving platform.

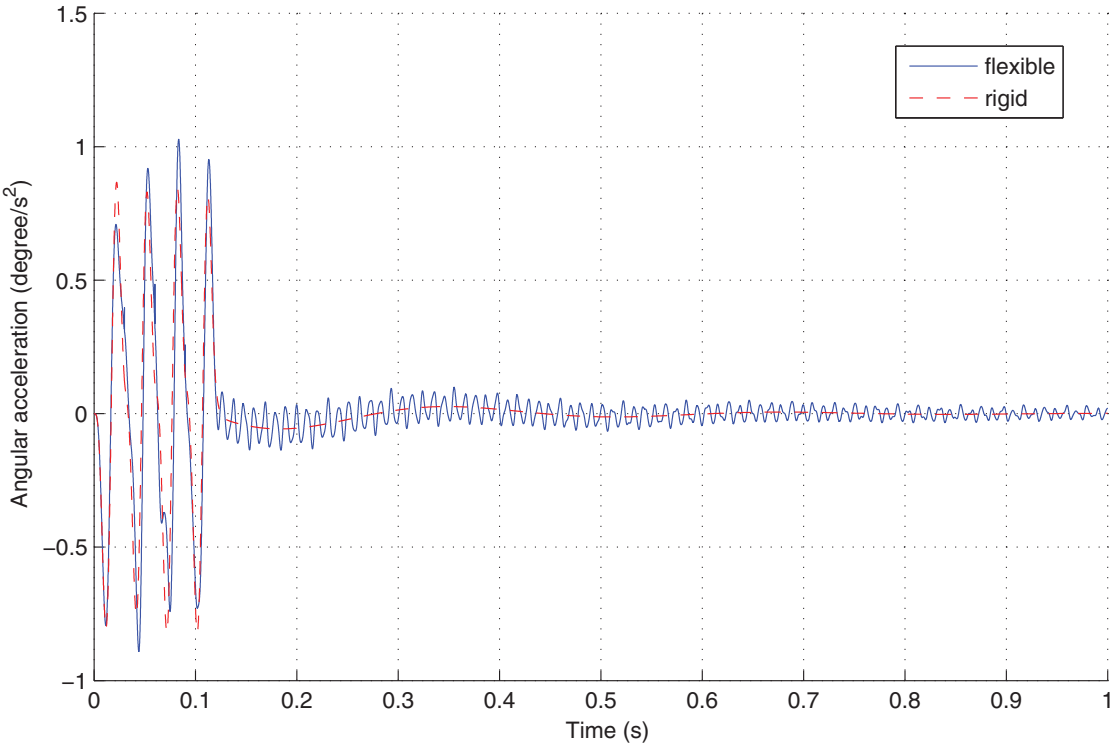


Fig. 10. Angular acceleration of the moving platform.

assumed as $\varsigma_1 = 0.047$ and $\varsigma_2 = 0.017$. Then the parameters of the ZVD input shaper are derived as follows:

$$\begin{bmatrix} A_i^1 \\ t_i^1 \end{bmatrix} = \begin{bmatrix} 0.2872 & 0.4837 & 0.2381 \\ 0 & 0.0074 & 0.0188 \end{bmatrix}, \quad \begin{bmatrix} A_i^2 \\ t_i^2 \end{bmatrix} = \begin{bmatrix} 0.2835 & 0.4696 & 0.2169 \\ 0 & 0.0085 & 0.0270 \end{bmatrix}. \tag{33}$$

As illustrated in Figs. 14 to 16, compared with only using the PD control, it is shown that the deflection of the linkages is significantly attenuated by adding the ZVD input shaper. The delay time

https://doi.org/10.1017/S026357471400023X Published online by Cambridge University Press

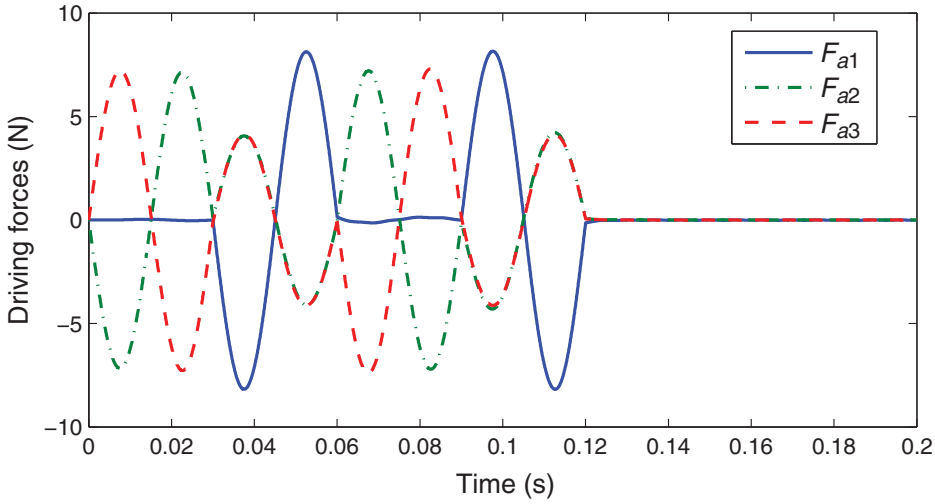


Fig. 11. Actuating forces provided by three LUSMs.

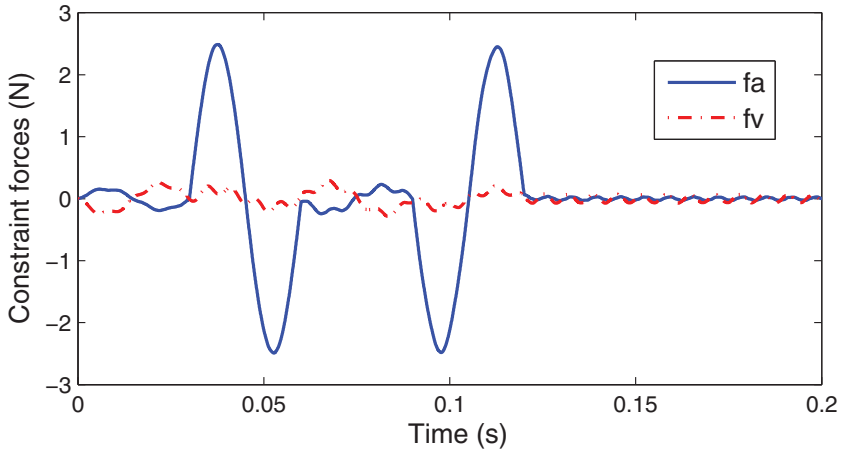


Fig. 12. Constraint forces applied at the tip of the first links.

is calculated as 0.0064 s, and considered to be acceptable since no significant effect is found in Figs 14 to 16. The vibration amplitude for each of the three links is different because of their different rigid-body motion and boundary condition excitations. In Figs. 17 and 18 vibrations of the first two modes of the first linkage are suppressed effectively by performing the PD control with input shaper. It is also demonstrated that the magnitude at the first natural frequency is much larger than the other two natural frequencies, which implies that the first mode is sufficient to model the deflection of elastic linkages.

Figures 19 and 20 are the comparison of the tracking errors of the moving platform between PD controller and PD controller with an input shaping controller. It is shown that during the trajectory tracking process, namely between 0 to 0.12 s, the tracking error is mainly caused by the PD controller, and the input shaper provides almost no contribution in reducing such control errors. However, after the motion stops, namely after 0.12 s, the residual vibration of the flexible links becomes a dominant error source, which can then be suppressed effectively by introducing the input shaping controller. To further analyze the relationship between the tracking error and the vibration of flexible links, a fast Fourier transform is carried out to provide a power spectrum density (PSD) plot of the tracking error. As shown in Figs. 21 and 22, the oscillation of the tracking error contains the frequency components of 4, 26, 45, and 71 Hz. The PSD at a frequency of 71 Hz, which is caused by the vibration of the flexible link, is significantly reduced by 67.3% when input shaping control is implemented.

https://doi.org/10.1017/S026357471400023X Published online by Cambridge University Press

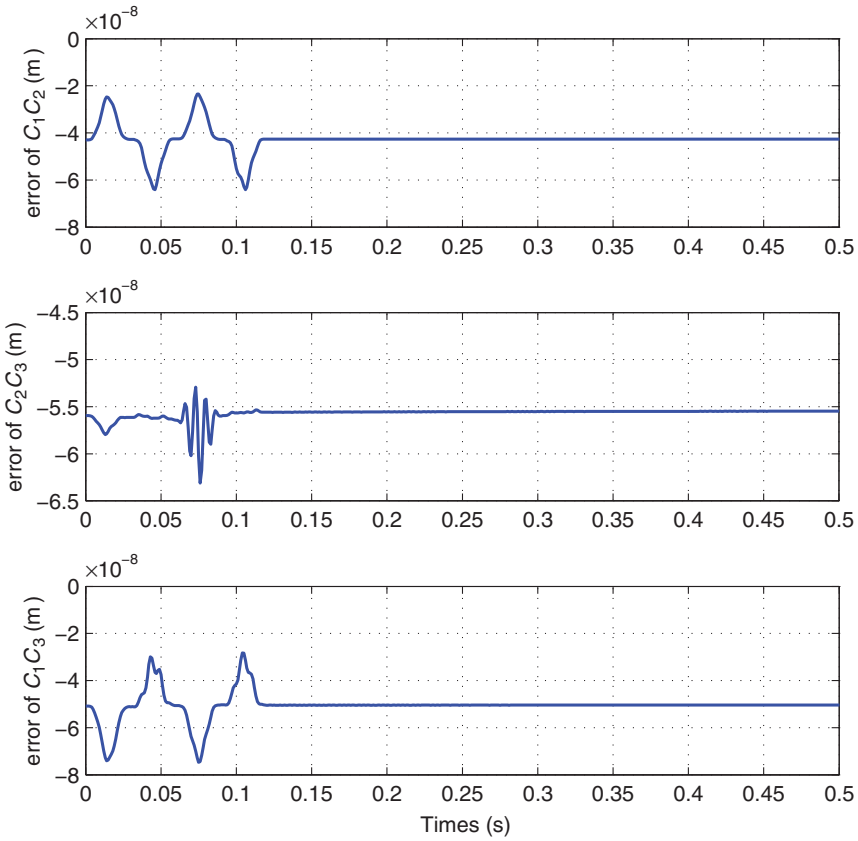


Fig. 13. Error of geometry constraint conditions among points C_i.

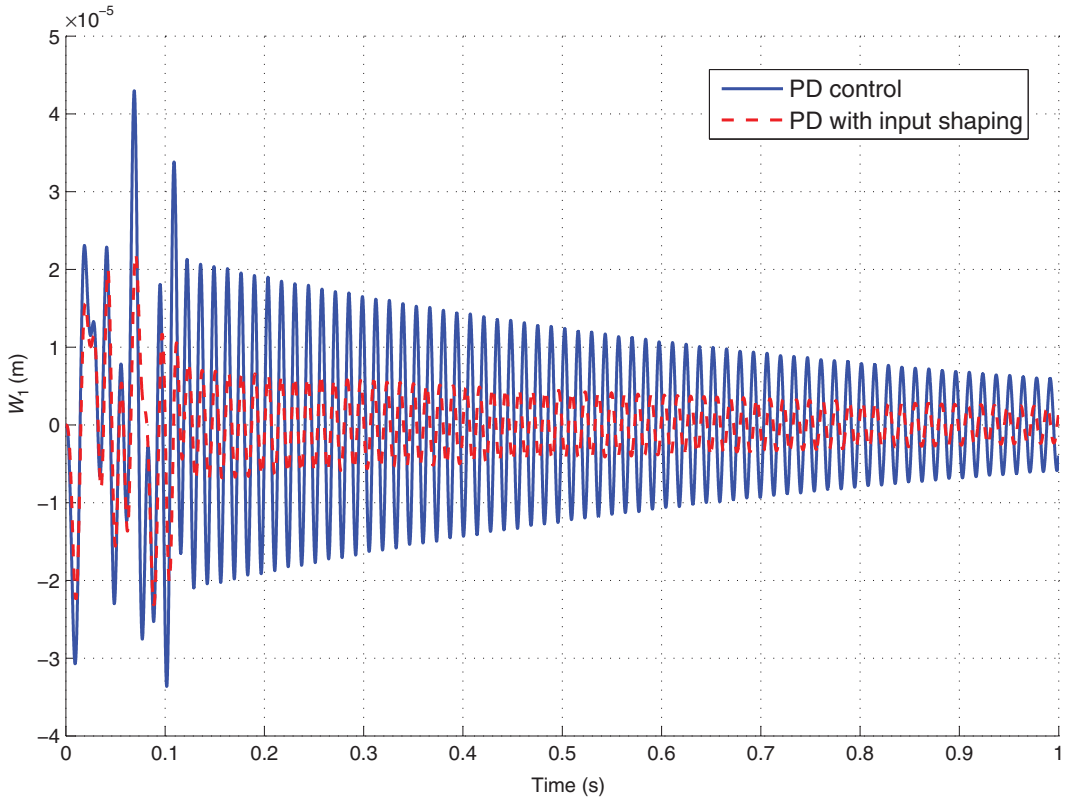


Fig. 14. Tip vibration of the first flexible linkage.

https://doi.org/10.1017/S026357471400023X Published online by Cambridge University Press

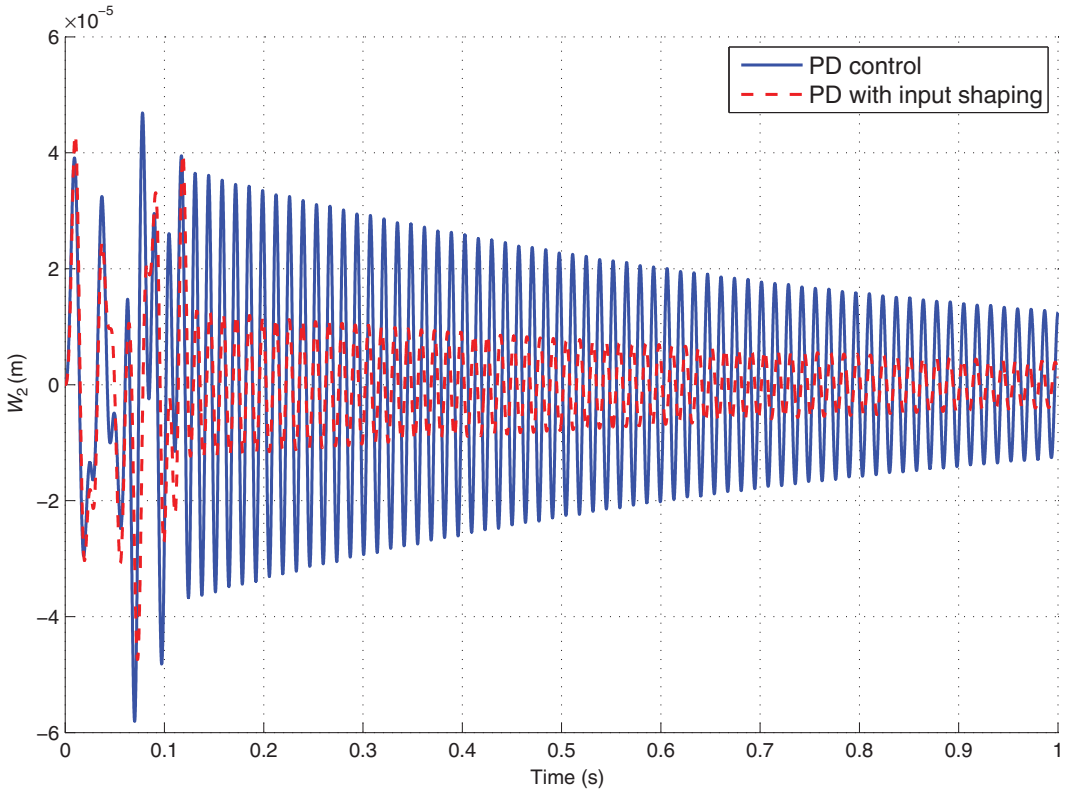


Fig. 15. Tip vibration of the second flexible linkage.

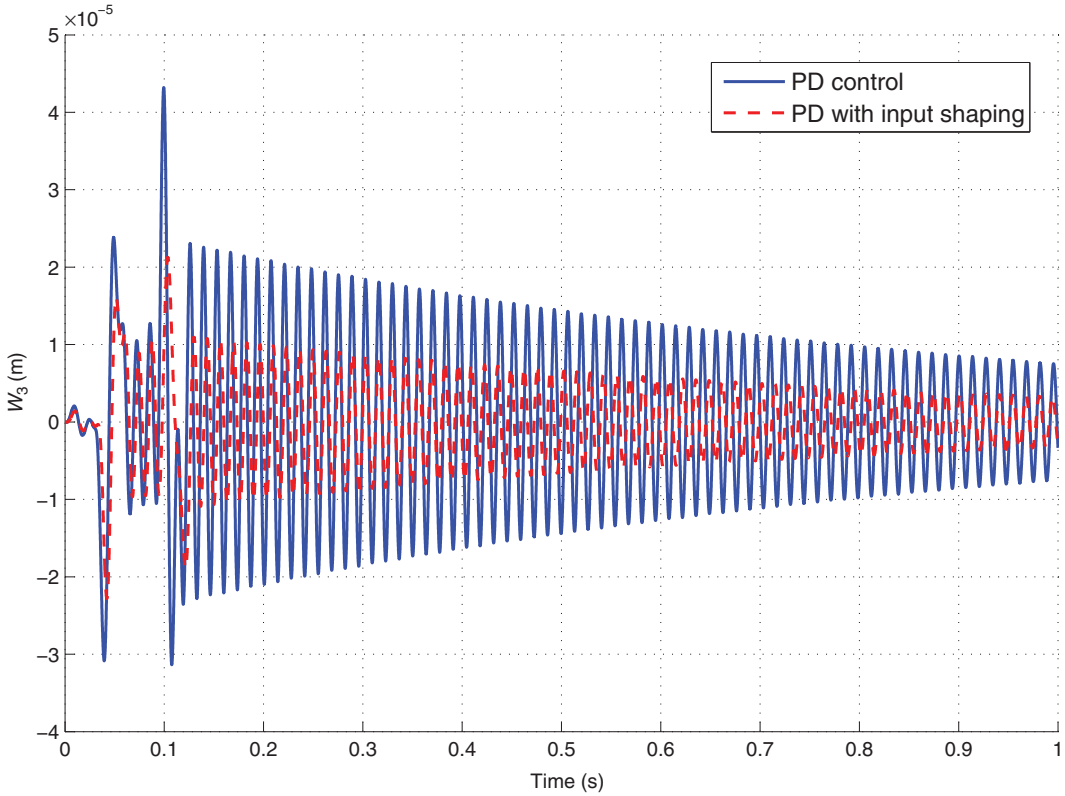


Fig. 16. Tip vibration of the third flexible linkage.

https://doi.org/10.1017/S026357471400023X Published online by Cambridge University Press

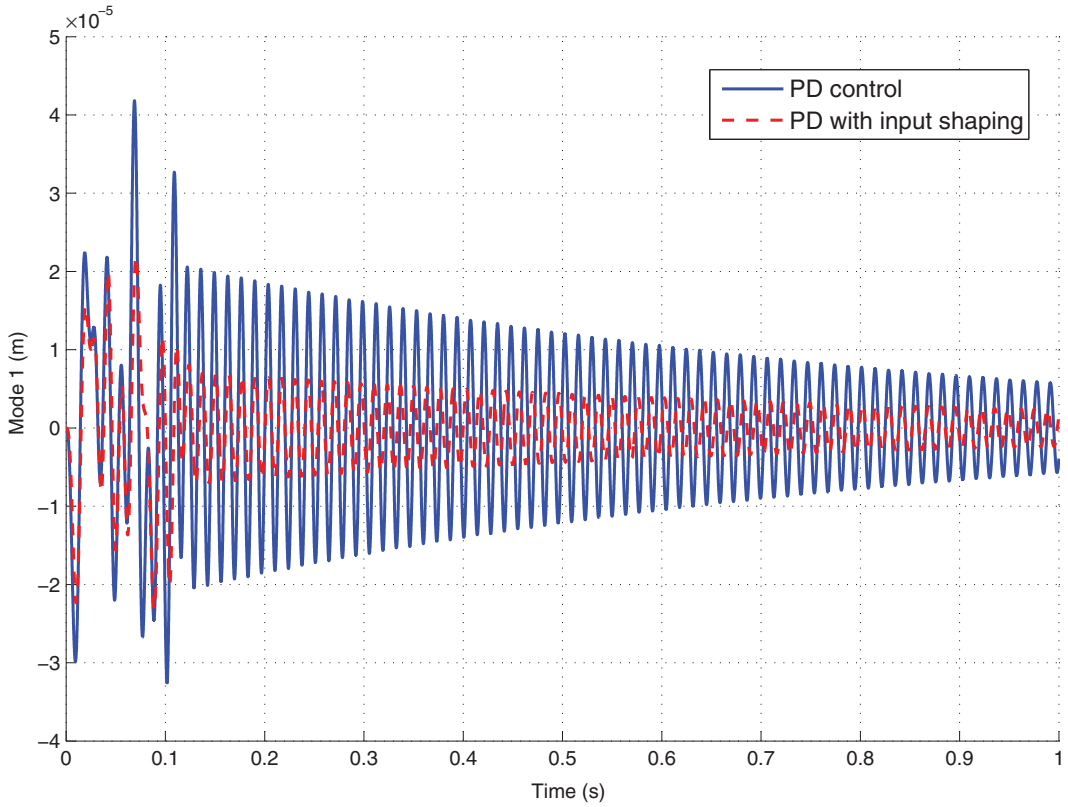


Fig. 17. The first mode vibration at the tip of the first flexible linkage.

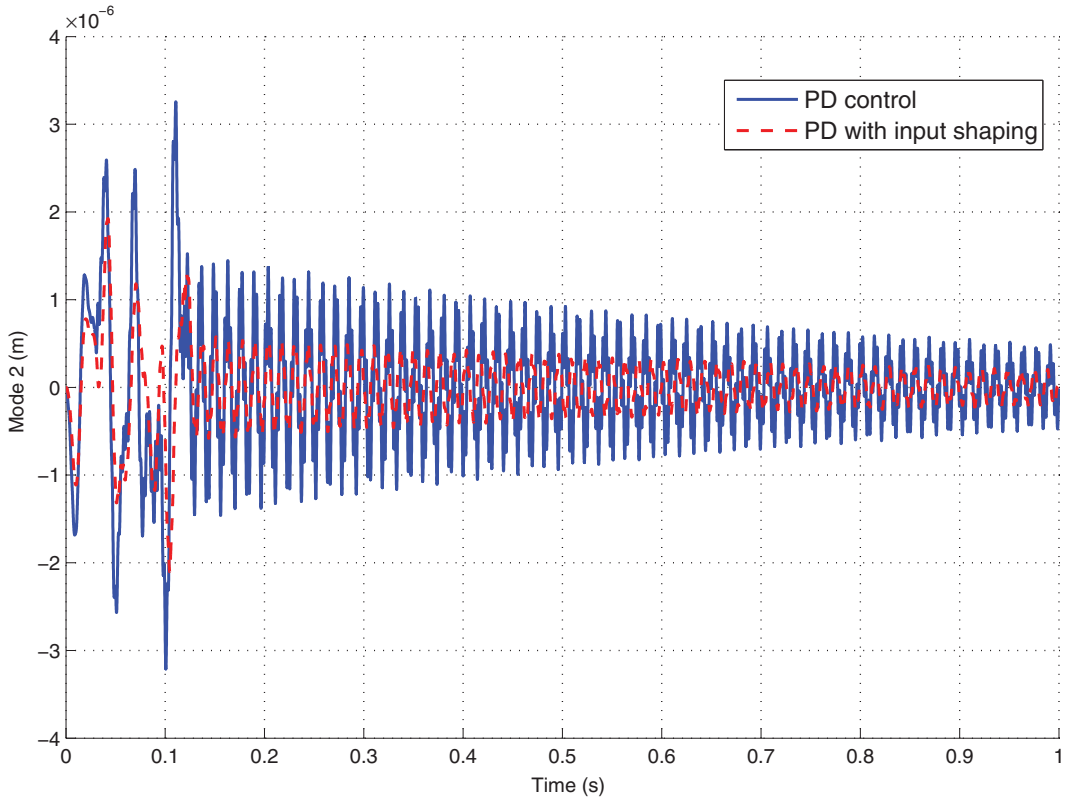


Fig. 18. The second mode vibration at the tip of the first flexible linkage.

https://doi.org/10.1017/S026357471400023X Published online by Cambridge University Press

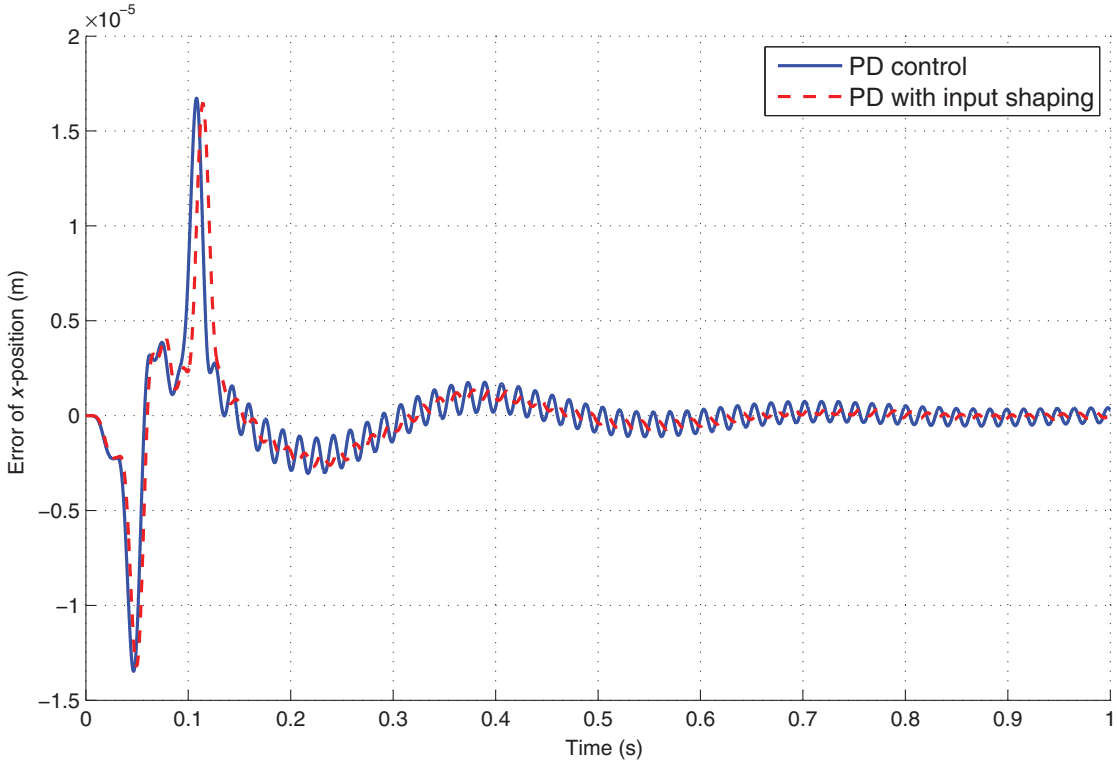


Fig. 19. Tacking error of a moving platform along the x-axis with input shaping control.

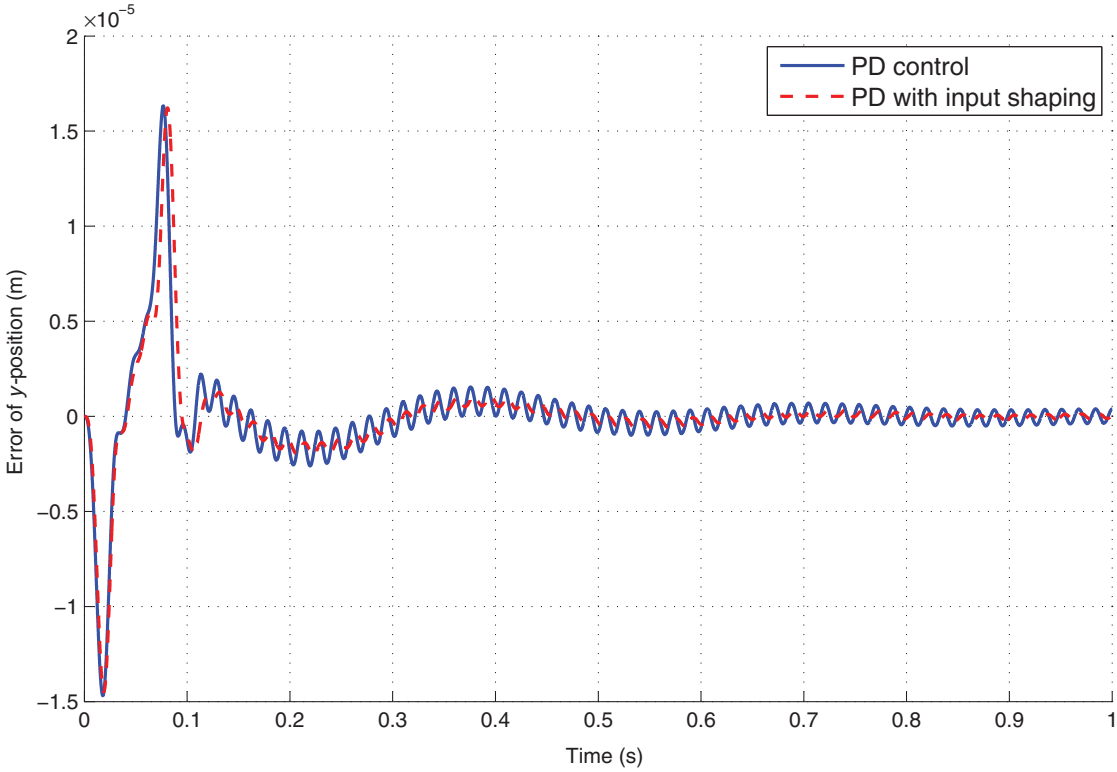


Fig. 20. Tacking error of a moving platform along the y-axis with input shaping control.

https://doi.org/10.1017/S026357471400023X Published online by Cambridge University Press

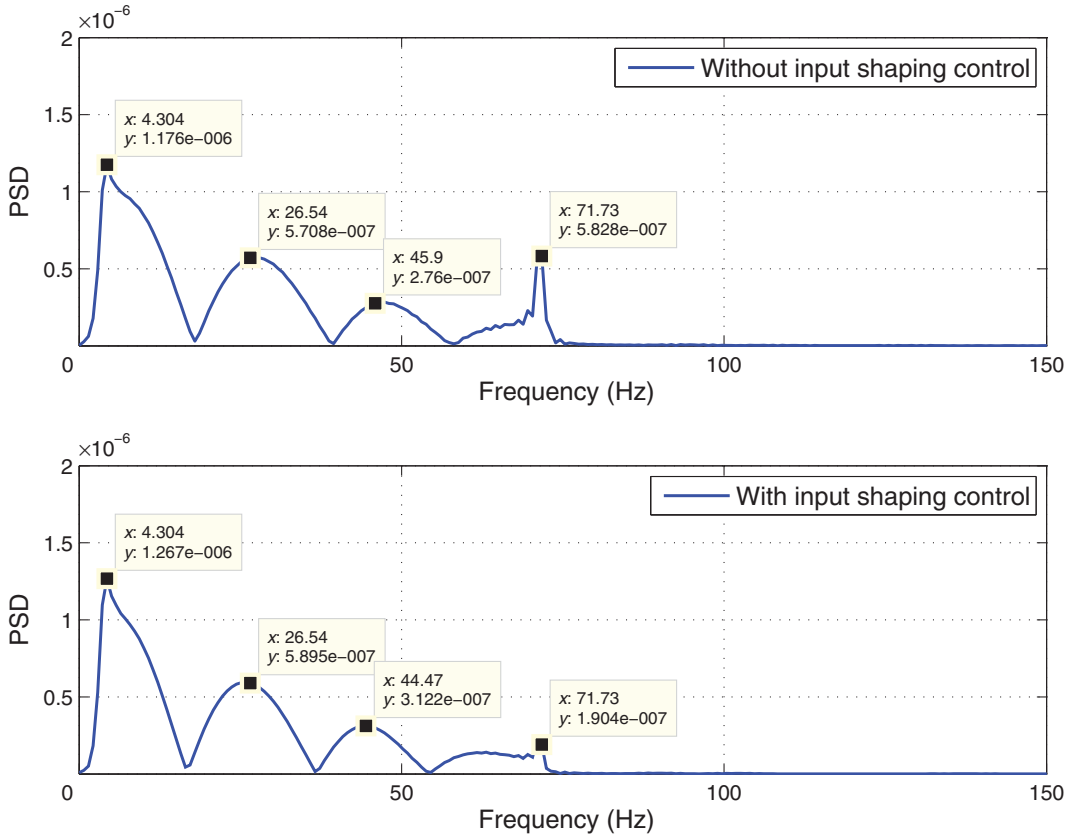


Fig. 21. FFT of the tracking error of a moving platform along the *x*-axis.

However, the PSD at other frequencies remains almost unchanged, since the input shaping controller cannot reduce the error caused by the PD controller, as shown in Figs. 19 to 22. These results further validate the effectiveness of the input shaping controller in such a flexible parallel-structure manipulator. Although we can conclude from Figs. 14 to 22 that the oscillation of the tracking error along the *x*- and *y*-axes is caused by the vibration of flexible links, a small difference between the frequency of the oscillation of the tracking error (71.7 Hz) and the dominant frequency of flexible links (79.5 Hz) is seen. These differences are likely due to the coupled nature of the parallel structure of the manipulator and the unmodeled dynamics.

6. Experimental Validation

6.1. Modal test experiment

Experimental modal test is implemented to validate the assumed mode shape and natural frequencies of flexible links. During the test, the moving platform is located at its initial configuration, namely the three LUSMs are locked at their home position. The accelerometer (PCB 333B32) is bonded sequentially on flexible linkage from points 1 to 10, and the impact hammer (PCB 086B02) is used to excite oscillation at point 2 of the first linkage, as shown is Fig. 23. The experiment is conducted for 15 times for each location of the accelerometer to obtain an average result. The vibration properties of the flexible linkage are analyzed and identified based on the dynamic response analyzer (Agilent 35670A). We found that the vibrations at point 8 (at 150 mm) and point 5 (at 90 mm) of flexible links are almost zero due to the nodes of the first and second mode shapes, respectively. These results match well with the assumption of pinned-free boundary condition. Detailed analyses are presented in ref. [34]. Based on the analysis of the measured frequency response functions (FRFs), the first two mode shapes are validated, as illustrated in Fig. 24. The first natural frequency is 92.5 Hz with a damping ratio of 0.041, and the second frequency is 241.3 Hz with a damping ratio of 0.013. However, a small

https://doi.org/10.1017/S026357471400023X Published online by Cambridge University Press

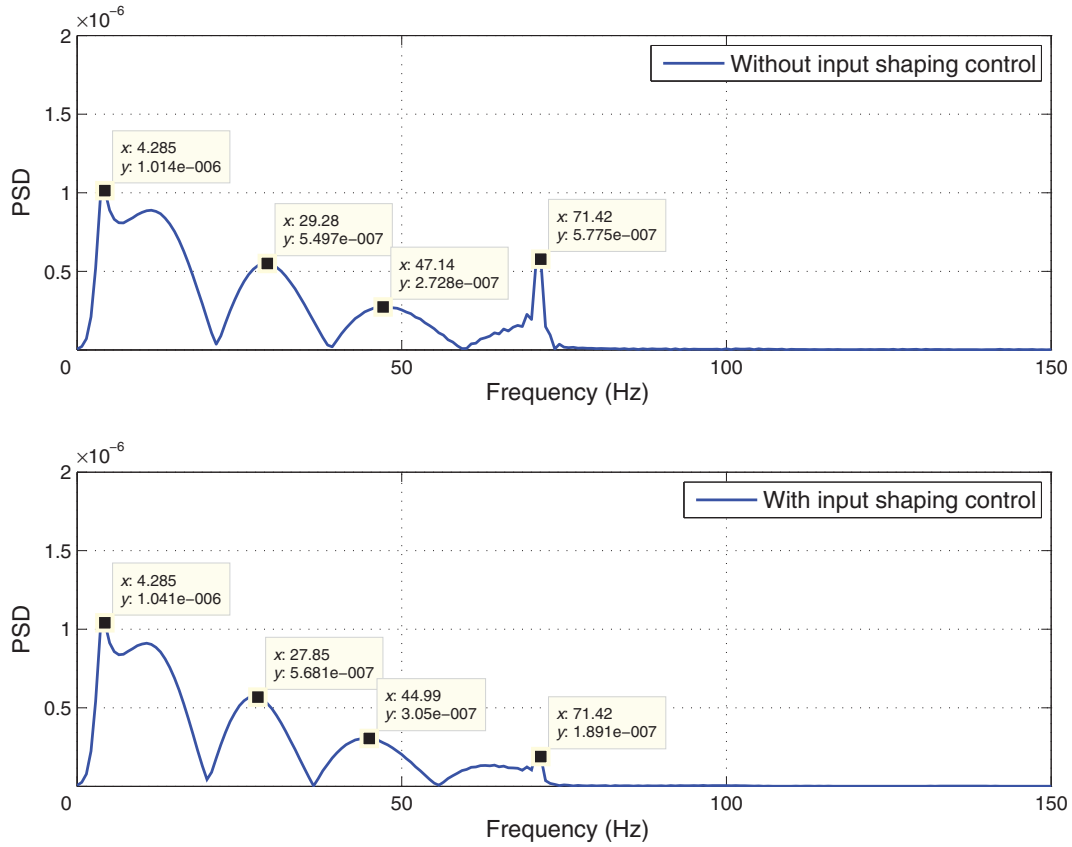


Fig. 22. FFT of the tracking error of a moving platform along the *y*-axis.

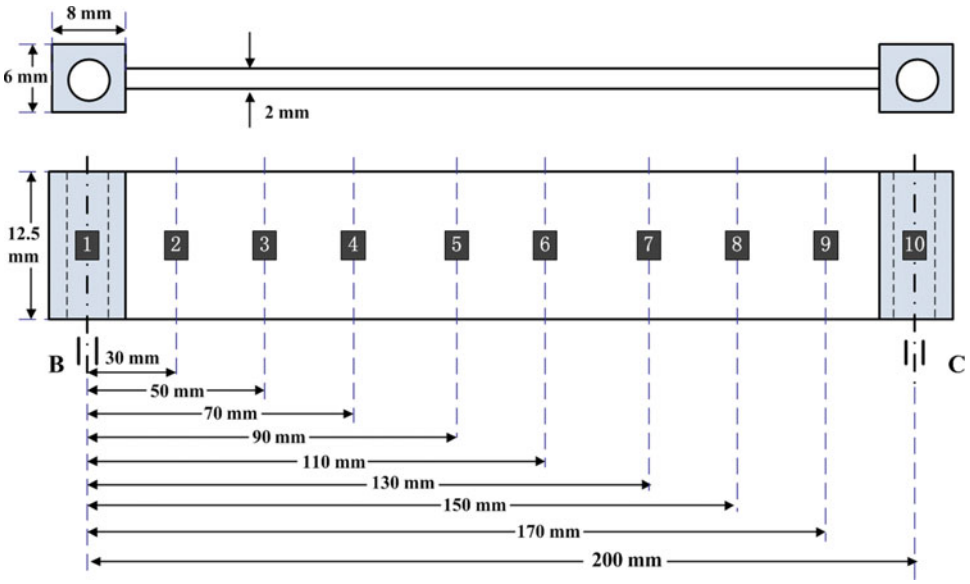


Fig. 23. Arrangement of accelerometer location.

difference between the measured mode shapes and the assumed mode shapes at the end of flexible links is seen. This is mainly due to the end of the flexible link subject to the constraint forces applied by joint C_i rather than a free endpoint. The constraint forces are related to the variation of speed, acceleration, and the loading of PPM. Hence, the mode shapes of the pinned-free conditions are much

https://doi.org/10.1017/S026357471400023X Published online by Cambridge University Press

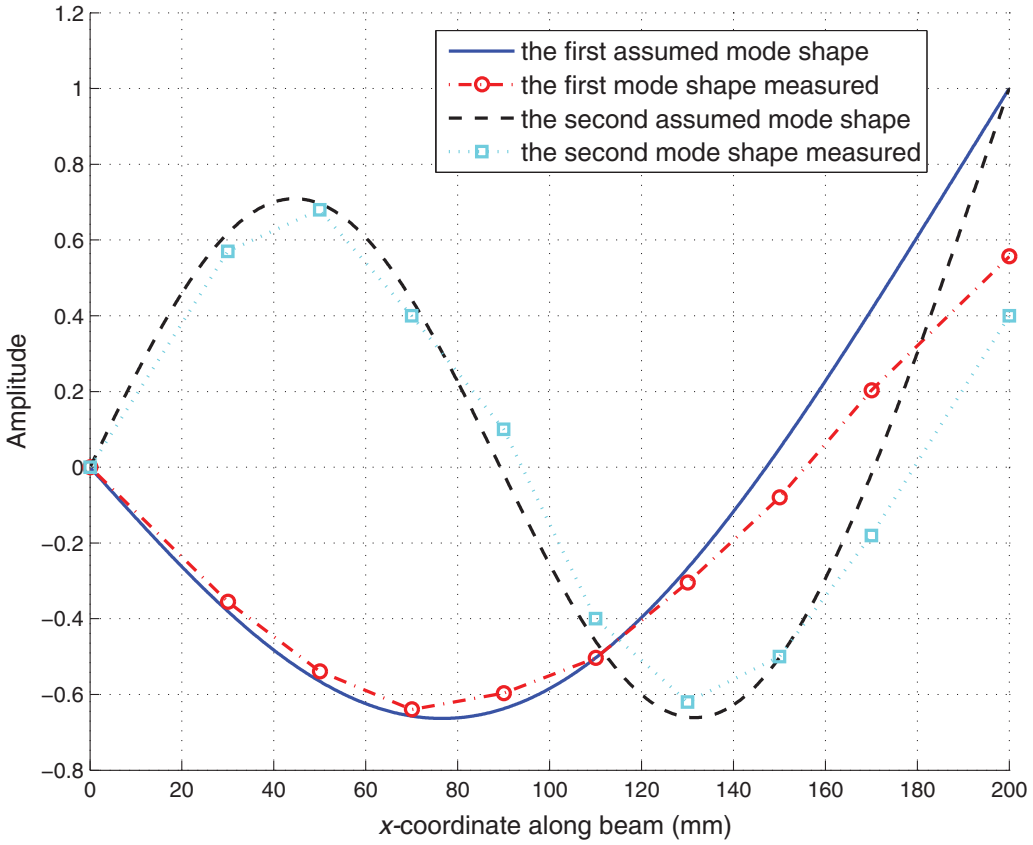


Fig. 24. The first two mode shapes of the flexible link identified.

closer to the actual conditions, compared with the pinned–pinned boundary conditions, which further explains why the moving platform generates vibration during the operation.

6.2. Experiment results of input shaping control

Experiments with and without input shaper are implemented in this section. The natural frequencies and damping ratios identified by modal analysis experiments are adopted to design the input shaper. The trajectory of the moving platform, the controller gain, and other parameters are identical to those derived in Sections 4 and 5. An experimental system has been built to carry out the PD feedback with input shaping control investigations, as shown in Fig. 25. The motion control card (DMC-1842, GALIL) is used to control the three LUSMs through LUSM drivers (made by NUAA). The feedback signal is provided by the linear grating sensor (LIA20, NUMERIK JENA). Two PZT sensors (PZT5 and CSSC) mounted on the quarter and three-quarter points of each flexible linkage are used to track vibration response, and the response voltage is processed by the data acquisition card (PCI-1710, Advantech Corporation). The sample time is set at 0.001 s. The CPU of the control PC is Core-i5-2400 (Microsoft) with a main calculation frequency of 3.1 GHz, which is fast enough to perform the real-time control.

To guarantee the accuracy of the proposed control algorithm, a kinematic calibration is performed before the control experiment. First of all, a set of N postures of the moving platform with $\overline{X}_p^n = (x_p^n, y_p^n, \varphi_p^n)^T$ is chosen. Second, the N postures of the moving platform are substituted into the ideal kinematic equations, namely Eqs. (1) and (2), to generate N corresponding ideal positions of LUSMs with $\bar{\rho}^n = (\rho_1^n, \rho_2^n, \rho_3^n)$. Noting that in the calibration procedures the elastic motions of $w_i(L_i)$ in Eqs. (1) and (2) are equal to zero, since the real postures of the moving platform will be detected after the residual vibration disappears. Then by driving the LUSMs to the N ideal positions, N corresponding real postures of the moving platform with $\overline{X}_p^{nr} = (x_p^{nr}, y_p^{nr}, \varphi_p^{nr})^T$ are obtained using CCD cameras.

https://doi.org/10.1017/S026357471400023X Published online by Cambridge University Press

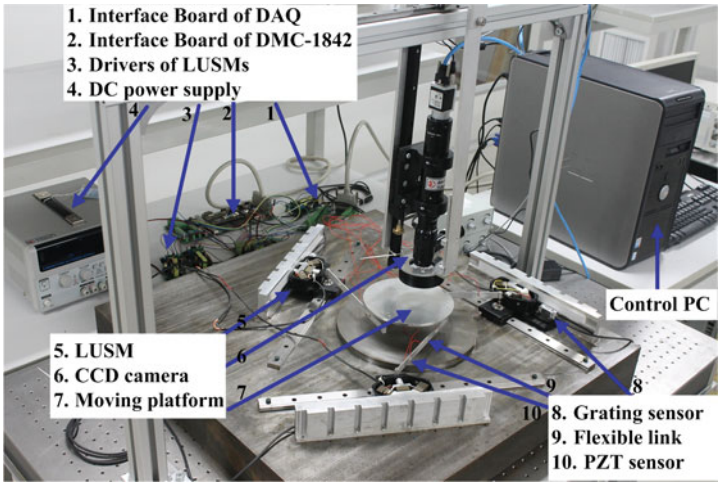


Fig. 25. Photograph of an input shaping control experiment setup.

Finally, the particle swarm optimization (PSO) algorithm[39] is adopted to minimize the error cost function J_E to obtain the real kinematic parameters. The error cost function J_E is given as

$$J_E = \sum_{j=1}^{n} \boldsymbol{E}_j^{\mathrm{T}} \boldsymbol{E}_j = \sum_{j=1}^{n} \left\| \boldsymbol{E}_j \right\|^2, \tag{34}$$

where $\boldsymbol{E} = [E_1\ E_2\ E_3]^T$;

$$E_i = \rho_i - (x_{Ci} - x_{Ai})\cos\alpha_i - (y_{Ci} - y_{Ai})\sin\alpha_i + \sqrt{L_i^2 - [(x_{Ci} - x_{Ai})\sin\alpha_i - (y_{Ci} - y_{Ai})\cos\alpha_i]^2};$$

$$\bar{X}_{Ci} = (x_{Ci}, y_{Ci}) = (x_p + x'_{ci}\cos\varphi_p - y'_{ci}\sin\varphi_p,\ y_p + x'_{ci}\sin\varphi_p + y'_{ci}\cos\varphi_p).$$

Acquiring 100 postures of the moving platform in the workspace and implementing the above-mentioned calibration procedure, yields the following calibrated kinematic parameters as shown in Table I.

In the control experiments, two different control approaches, the PD controller with and without input shaper, are conducted as a comparison. The time response of the PZT sensors bonded at the quarter point of each flexible link are displayed in Figs. 26 to 28. The time response has units in volts, and the PZT sensors have a sensitivity of 0.25 V/$\mu\varepsilon$. It is demonstrated that the vibrations of the three links are attenuated effectively by adding the input shaper, and the experimental results are also in agreement with the simulation plots illustrated in Figs. 14 to 16. For further analysis, the PSD plot of the response of the PZT sensor bonded at the quarter of the first link is provided. As shown in Fig. 29, the PSD at the first mode frequency is significantly reduced by 34.5% when input shaping control is implemented, and the vibration at the second mode frequency remains almost unchanged, since the second mode has a very low level of PSD, which would be easily affected by noise. This further provides validation that the vibration of the first mode is the dominant vibration, and much attention should be paid to suppress the first-order modal vibration. It is demonstrated in Fig. 29 that the vibration of the elastic linkage contains the frequency components of 33.1, 64.2, 90.82, 145.5, and 234.4 Hz, which means that it also contains other frequency components, other than the natural frequencies. These other frequencies likely result from the actuation force of the LUSM, vibration of the LUSM, and coupling effects between the rigid joint motion and the flexible linkage. However, the coupled vibration characteristics between the natural and the forced frequencies result in a fair more complex dynamic analysis of the PPM. However, compared with a single flexible link manipulator,

https://doi.org/10.1017/S026357471400023X Published online by Cambridge University Press

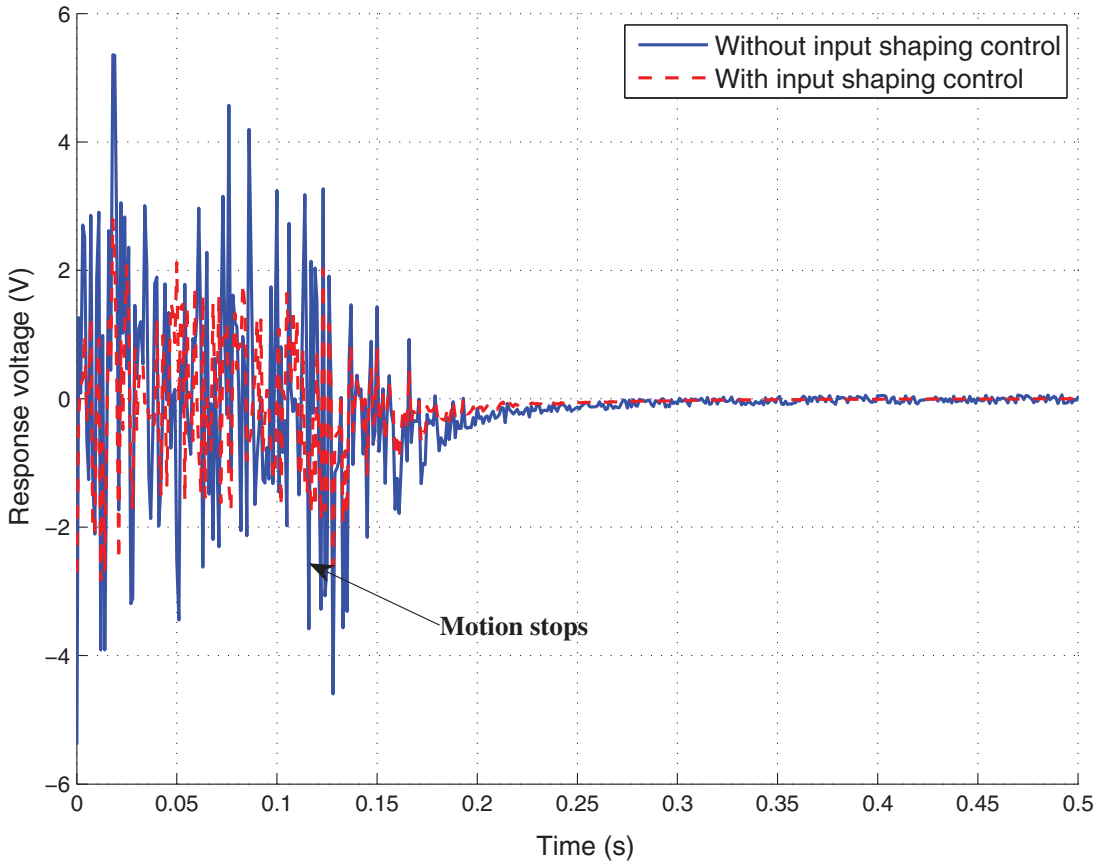


Fig. 26. Response of PZT sensor mounted at the quarter of the first link.

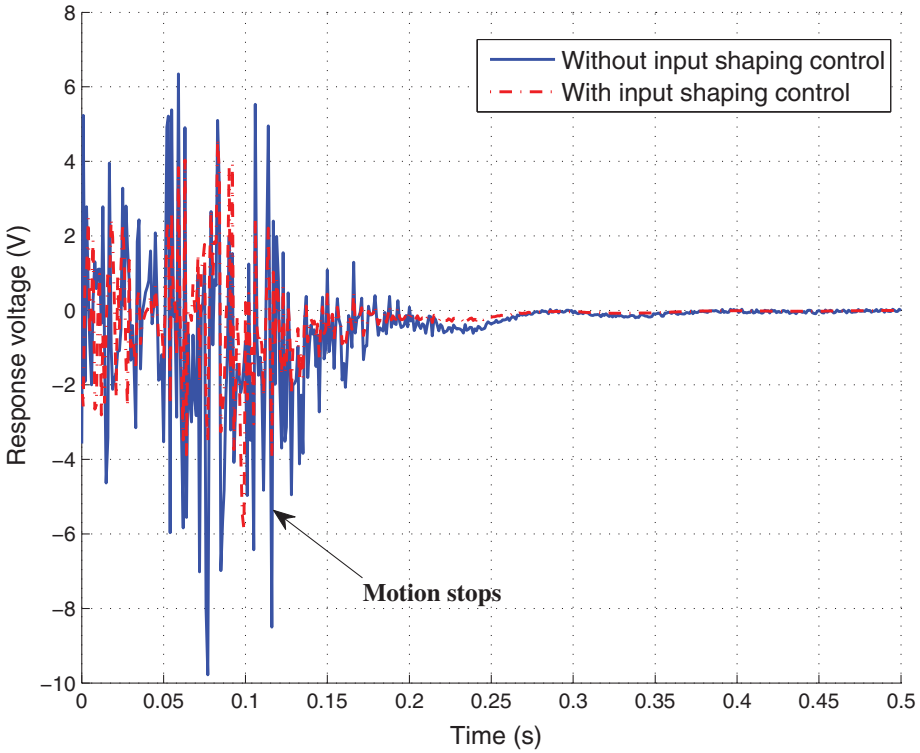


Fig. 27. Response of PZT sensor mounted at the quarter of the second link.

https://doi.org/10.1017/S026357471400023X Published online by Cambridge University Press

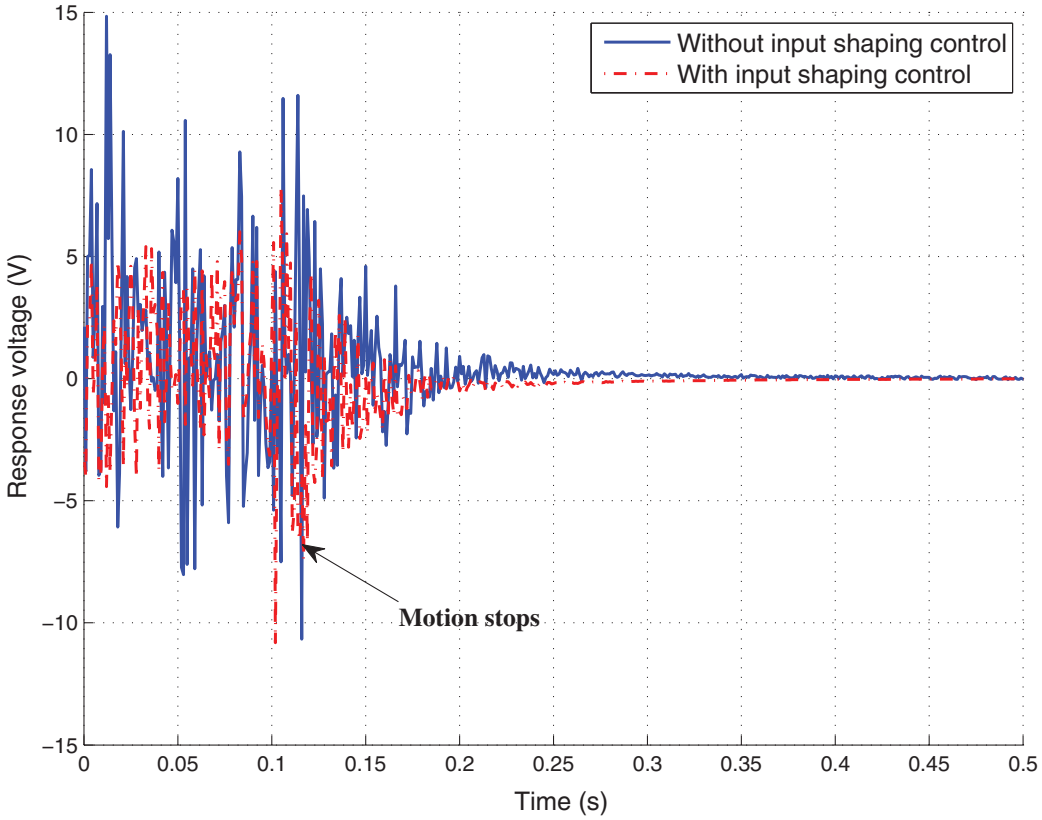


Fig. 28. Response of PZT sensor mounted at the quarter of the third link.

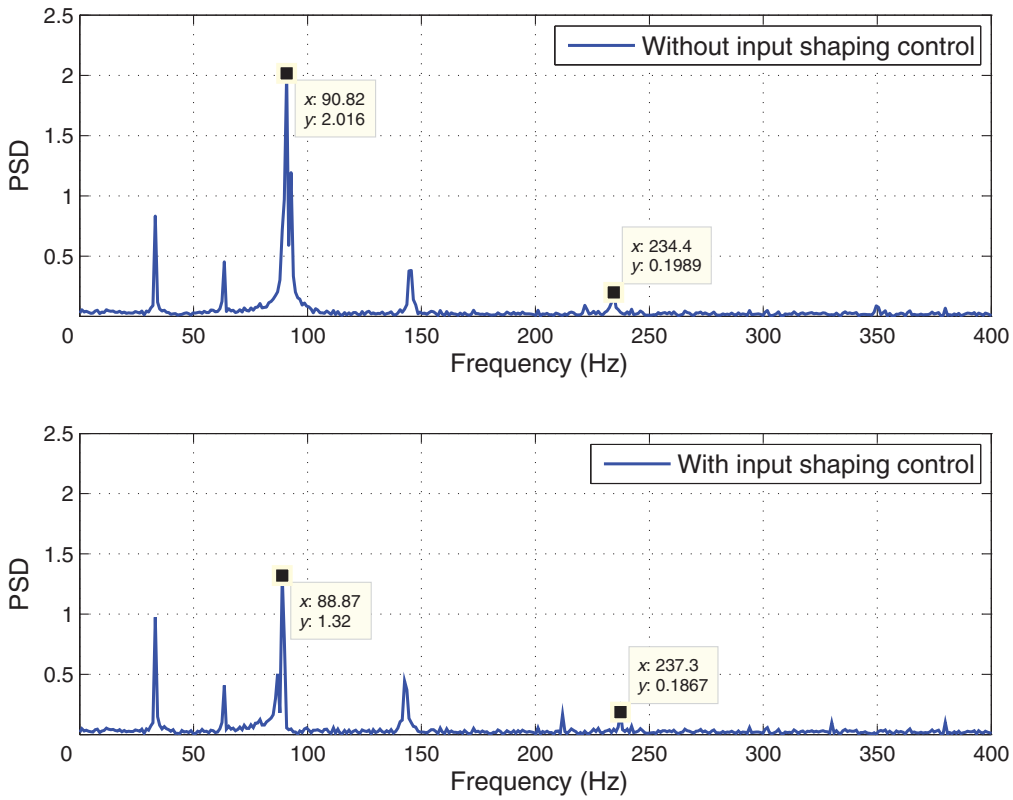


Fig. 29. FFT of the PZT sensor mounted at the quarter of the first link.

https://doi.org/10.1017/S026357471400023X Published online by Cambridge University Press

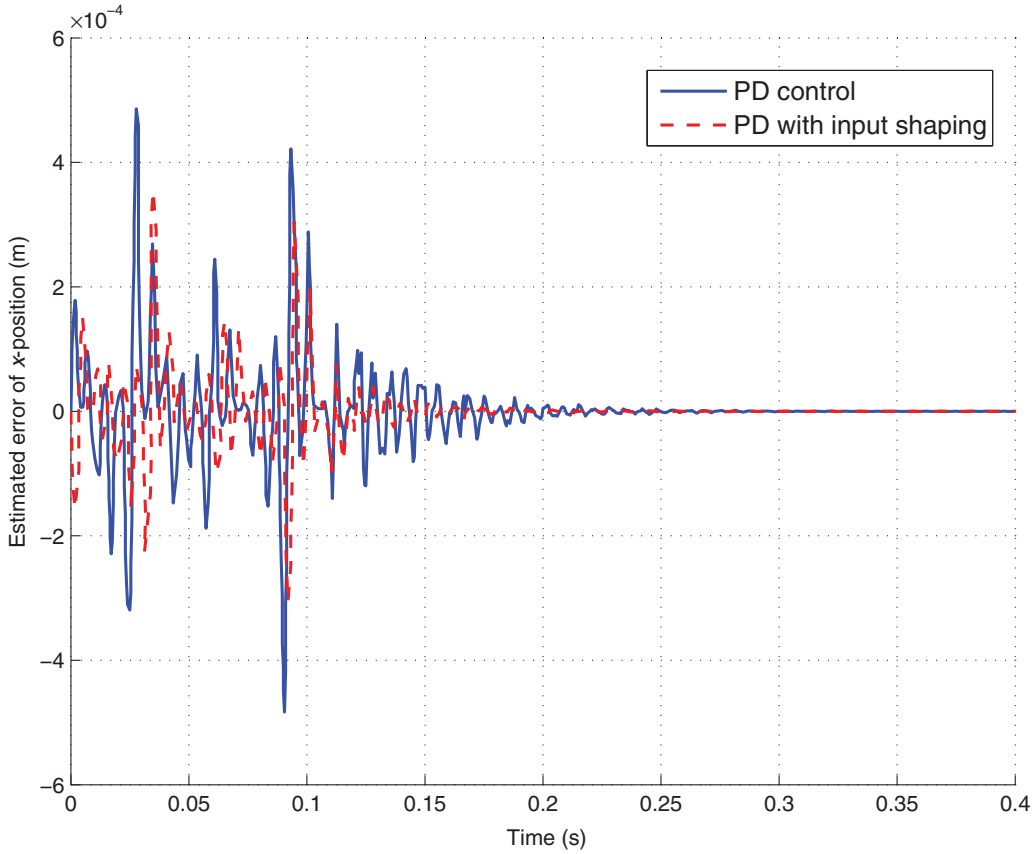


Fig. 30. Estimated error of the moving platform along x-axis.

in which the residual vibration can be completely eliminated with the input shaping method, the input shaper here in the parallel structure manipulator can only reduce part of the residual vibration due to the highly coupled nature between the rigid and elastic motions. Therefore, other vibration control approaches, such as singular perturbation method and active vibration control method based on multiple PZT transducers, may be required to combine with the input shaper to achieve further vibration suppression.

The CCD camera adopted in the experimental system is used to provide a closed-loop feedback signal for calibration work and positioning control with an image capture rate of 30 frames per second, and hence the complete tracking error may not be captured with the CCD camera since the vibration frequencies of the flexible link and the moving platform are much higher than the image capture rate. According to ref. [38], an approach is proposed to estimate the tracking error of the moving platform using the output voltages of PZT sensors mounted on flexible links and feedback signals of a linear grating sensor. Equation (19) is used to estimate the tracking error along x- and y-axes. The modal coordinates $\bar{q}$ in Eq. (19) are calculated using the output voltages of PZT sensors through a modal filter,[38] and the variables $\ddot{\bar{q}}$ and $\dot{\bar{q}}$ in Eq. (19) can be obtained by differentiating $\bar{q}$ twice and once, respectively. Similarly, the variables $\ddot{\bar{\rho}}$ and $\dot{\bar{\rho}}$ in Eq. (19) are computed by differentiating signals from linear grating sensors twice and once, respectively. Then integrating Eq. (19) twice and subtracting the ideal trajectory yields the estimated tracking error of the moving platform, as shown in Figs. 30 and 31. The estimated tracking error shows that the errors of the moving platform are reduced due to the implementation of the input shaping controller, especially for the residual oscillation of the moving platform after the rigid motion stops. This is mainly because the vibration of the flexible link becomes a dominant error source of the moving platform after the rigid motion stops. The peaks in Figs. 30 and 31 are due to direction changes at the corners of the squared trajectory. These results are consistent with the simulation results, as shown in Figs. 19 and 20.

https://doi.org/10.1017/S026357471400023X Published online by Cambridge University Press

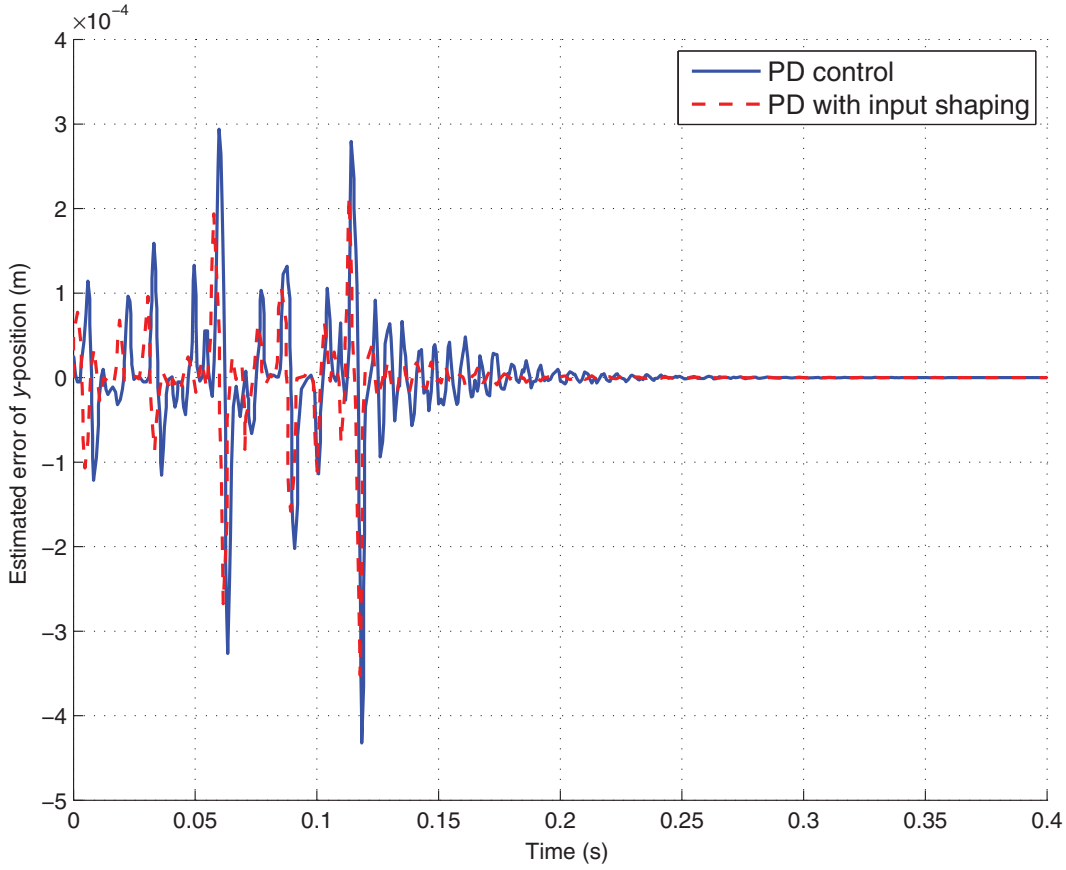


Fig. 31. Estimated error of the moving platform along *y*-axis.

7. Conclusions

This paper addresses the dynamic modeling of a rigid–flexible PPM with flexible linkage driven by LUSMs. The sub-structure methodology and the extended Hamilton's principle are employed to formulate the rigid–flexible dynamic model with actual boundary conditions. Compared with the KED assumption, the proposed dynamic model considered the interaction between the rigid and elastic dynamics. The PD feedback control incorporated with the input shaping control is designed to achieve trajectory while suppressing the residual vibration. Computer simulation and experiments are presented to investigate the proposed dynamic model and the proposed controller. The modal test experiments have verified the assumptions used in the model. The input shaping control experiment shows that the residual vibration can be suppressed effectively, which provide a valuable contribution to the vibration attenuation of such flexible PPM through joint motion control.

Acknowledgments

This work was supported by the National Natural Science Foundation of China (grant numbers: 91223201, 51375225, 51275235, and 51175264), the Natural Science Research Project of Jiangsu (grant number: BK2012797), the Fundamental Research Funds for the Central Universities (grant number: NE2013001), the Priority Academic Program Development of Jiangsu Higher Education Institutions, and also with support from the NSERC Discovery Grants of J.K. Mills and W.L. Cleghorn. The authors would also like to thank the reviewers and the editor for their efforts in improving the paper.

References

1. J.-P. Merlet, *Parallel Robots* (Springer, New York, NY, 2006).
2. C. Zhao, *Ultrasonic Motors* (Springer-Verlag, Berlin, Germany, 2011).

https://doi.org/10.1017/S026357471400023X Published online by Cambridge University Press

3. Y. Shi, Y. Li, C. Zhao and J. Zhang, "A new type butterfly-shaped transducer linear ultrasonic motor," *J. Intell. Mater. Syst. Struct.* **22**(6), 567–575 (2011).
4. M. Korayem, A. Heidari and A. Nikoobin, "Maximum allowable dynamic load of flexible mobile manipulators using finite element approach," *Int. J. Adv. Manuf. Technol.* **36**(5–6), 606–617 (2008).
5. R. C. Winfrey, "Elastic link mechanism dynamics," *J. Eng. Ind.* **93**, 268 (1971).
6. M. A. Ahmad, Z. Mohamed and N. Hambali, "Dynamic Modelling of a Two-Link Flexible Manipulator System Incorporating Payload," *Proccedings of 3rd IEEE Conference on Industrial Electronics and Applications (ICIEA 2008)*, Singapore (2008) pp. 96–101.
7. M. Loudini, D. Boukhetala and M. Tadjine, "Comprehensive mathematical modelling of a lightweight flexible link robot manipulator," *Int. J. Modelling, Identif. Control* **2**(4), 313–321 (2007).
8. L. Meirovitch and R. Parker, "Fundamentals of vibrations," *Appl. Mech. Rev.* **54**, 100 (2001).
9. X. Zhang, J. K. Mills and W. L. Cleghorn, "Dynamic modeling and experimental validation of a 3-PRR parallel manipulator with flexible intermediate links," *J. Intell. Robot. Syst.* **50**(4), 323–340 (2007).
10. A. De Luca and B. Siciliano, "Closed-form dynamic model of planar multilink lightweight robots systems," *IEEE Trans. Man Cybern.* **21**(4), 826–839 (1991).
11. K. Krishnamurthy and L. Yang, "Dynamic modeling and simulation of two cooperating structurally flexible robotic manipulators," *Robotica* **13**(4), 375–384 (1995).
12. M. O. Tokhi and A. M. Azad, *Flexible Robot Manipulators: Modelling, Simulation and Control* (Institution of Engineering and Technology, UK, 2008).
13. S. K. Dwivedy and P. Eberhard, "Dynamic analysis of flexible manipulators, a literature review," *Mech. Mach. Theory* **41**(7), 749–777 (2006).
14. X. Wang and J. K. Mills, "Substructuring Dynamic Modeling and Active Vibration Control of a Smart Parallel Platform," *Proccedings of 2004 ASME International Mechanical Engineering Congress*, Anaheim, CA, (2004) pp. 1–8.
15. Y.-Q. Yu, Z.-C. Du, J.-X. Yang and Y. Li, "An experimental study on the dynamics of a 3-RRR flexible parallel robot," *IEEE Trans. Robot.* **27**(5), 992–997 (2011).
16. S.-Z. Liu, Y.-Q. Yu, Z.-C. Zhu, L.-Y. Su and Q.-B. Liu, "Dynamic modeling and analysis of 3-RRS parallel manipulator with flexible links," *J. Cent. South Univ. Technol.* **17**(2), 323 (2010).
17. X. Zhang, J. K. Mills and W. L. Cleghorn, "Study on the Effect of Elastic Deformations on Rigid Body Motions of a 3-PRR Flexible Parallel Manipulator," *Proceedings of the International Conference on Mechatronics and Automation*, Harbin, P.R. China (2007) pp. 1805–1810.
18. J. Hu, P. Li and X. Cui, "Active Vibration Control of a High-Speed Flexible Robot Using Variable Structure Control," *Fifth International Conference on Intelligent Computation Technology and Automation*, Zhangjiajie, Hunan, P.R. China (2012) pp. 57–60.
19. T. Sun, Y.-M. Song and K. Yan, "Kinetostatic analysis of a novel high-speed parallel manipulator with rigid–flexible coupled links," *J. Cent. South Univ. Technol.* **18**(3), 593 (2011).
20. A. Shabana and R. Wehage, "Variable degree-of-freedom component mode analysis of inertia variant flexible mechanical systems," *J. Mech. Transm. Autom. Des.* **105**, 371–378 (1983).
21. F. Matsuno, T. Ohno and Y. V. Orlov, "Proportional derivative and strain (PDS) boundary feedback control of a flexible space structure with a closed-loop chain mechanism," *Automatica* **38**(7), 1201–1211 (2002).
22. T. Mansour, A. Konno and M. Uchiyama, "Modified PID control of a single-link flexible robot," *Adv. Robot.* **22**(4), 433–449 (2008).
23. M. Ahmad, M. Ramli, R. R. Ismail, N. Hambali and M. Zawawi, "The Investigations of Input Shaping with Optimal State Feedback for Vibration Control of a Flexible Joint Manipulator," *Proccedings of Conference on Innovative Technologies in Intelligent Systems and Industrial Applications*, Kuala Lumper, Malaysia (2009) pp. 446–451.
24. Y. Liu and D. Sun, "Stabilizing a flexible beam handled by two manipulators via PD feedback," *IEEE Trans. Autom. Control* **45**(11), 2159–2164 (2000).
25. Y. Su, D. Sun, L. Ren and J. K. Mills, "Integration of saturated PI synchronous control and PD feedback for control of parallel manipulators," *IEEE Trans. Robot.* **22**(1), 202–207 (2006).
26. B. Kang, B. Yeung and J. K. Mills, "Two-time scale controller design for a high-speed planar parallel manipulator with structural flexibility," *Robotica* **20**(5), 519–528 (2002).
27. N. C. Singer, "Residual Vibration Reduction in Computer Controlled Machines," *Ph.D. Dissertaion*, Massachusetts Institute of Technology, Cambridge, MA (1989).
28. T. Zhou, A. A. Goldenberg and J. W. Zu, "Modal Force Based Input Shaper for Vibration Suppression of Flexible Payloads," *Proceedings of IEEE International Conference on Robotics and Automation*, Washington DC (2002) pp. 2430–2435.
29. J. Shan, D. Sun and D. Liu, "Design for robust component synthesis vibration suppression of flexible structures with on-off actuators," *IEEE Trans. Robot. Autom.* **20**(3), 512–525 (2004).
30. W. E. Singhose and N. C. Singer, "Effects of input shaping on two-dimensional trajectory following," *IEEE Trans. Robot. Autom.* **12**(6), 881–887 (1996).
31. B. Li, X. Zhang, J. K. Mills, W. L. Cleghorn and L. Xie, "Vibration Suppression of a 3-PRR Flexible Parallel Manipulator Using Input Shaping," *International Conference on Mechatronics and Automation*, Changchun, Jilin, P.R. China (2009) pp. 3539–3544.
32. I. Heerah, B. Benhabib, B. Kang and J. K. Mills, "Architecture selection and singularity analysis of a three-degree-of-freedom planar parallel manipulator," *J. Intell. Robot. Syst.* **37**(4), 355–374 (2003).
33. S. Staicu, "Inverse dynamics of the 3-PRR planar parallel robot," *Robot. Auton. Syst.* **57**(5), 556–563 (2009).

https://doi.org/10.1017/S026357471400023X Published online by Cambridge University Press

34. Q. Zhang, J. K. Mills, W. L. Cleghorn, J. Jin and C. Zhao, "Trajectory tracking and vibration suppression of a 3-PRR parallel manipulator with flexible links," *Multibody Syst. Dyn.* 1–34 (2013). doi:10.1007/s11044-013-9407-2.
35. X. Zhang, J. K. Mills and W. L. Cleghorn, "Effect of Axial Forces on Lateral Stiffness of a Flexible 3-PRR Parallel Manipulator Moving with High-Speed," *International Conference on Information and Automation*, Zhangjiajie, Hunan, P.R. China (2008) pp. 1458–1463.
36. T. Zhou, J. W. Zu and A. A. Goldenberg, "Vibration Controllability of Flexible Robot-Payload Systems," *Proceedings of IEEE International Conference on Robotics and Automation*, San Francisco, CA (2000) pp. 1484–1489.
37. J. Shan, H.-T. Liu and D. Sun, "Modified Input Shaping for a Rotating Single-Link Flexible Manipulator," *J. Sound Vib.* **285**(1), 187–207 (2005).
38. X. Zhang, J. K. Mills and W. L. Cleghorn, "Multi-mode vibration control and position error analysis of parallel manipulator with multiple flexible links," *Trans. Can. Soc. Mech. Eng.* **34**(2), 197–213 (2010).
39. Z. Bingül and O. Karahan, "Dynamic identification of Staubli RX-60 robot using PSO and LS methods," *Expert Syst. Appl.* **38**(4), 4136–4149 (2011).

Appendix A

$$M_{11} = \begin{bmatrix} m_{S1} + m_{B1} + m_1 & 0 & 0 \\ 0 & m_{S2} + m_{B2} + m_2 & 0 \\ 0 & 0 & m_{S3} + m_{B3} + m_3 \end{bmatrix} \in R^{3\times 3},$$

$$M_{12} = \begin{bmatrix} \frac{m_1 L_1 S_1}{2} - C_1 \rho_{A1} \sum_{j=1}^{r} \int_0^{L_1} Y_{1j} q_{1j} dt & 0 & 0 \\ 0 & \frac{m_2 L_2 S_2}{2} - C_2 \rho_{A2} \sum_{j=1}^{r} \int_0^{L_2} Y_{2j} q_{2j} dt & 0 \\ 0 & 0 & \frac{m_3 L_3 S_3}{2} - C_3 \rho_{A3} \sum_{j=1}^{r} \int_0^{L_3} Y_{3j} q_{3j} dt \end{bmatrix} \in R^{3\times 3},$$

$$M_{14} = \begin{bmatrix} S_1 \int_0^{L_1} \rho_{A1} Y_{11} dx & \cdots & S_1 \int_0^{L_1} \rho_{A1} Y_{1r} dx & 0 & \cdots & 0 & 0 & \cdots & 0 \\ 0 & \cdots & 0 & S_2 \int_0^{L_2} \rho_{A2} Y_{21} dx & \cdots & S_2 \int_0^{L_2} \rho_{A2} Y_{2r} dx & 0 & \cdots & 0 \\ 0 & \cdots & 0 & 0 & \cdots & 0 & S_3 \int_0^{L_3} \rho_{A3} Y_{31} dx & \cdots & S_3 \int_0^{L_3} \rho_{A3} Y_{3r} dx \end{bmatrix} \in R^{3\times 3r},$$

$$M_{22} = \begin{bmatrix} \frac{m_1 L_1^2}{3} + J_{B1} & 0 & 0 \\ 0 & \frac{m_2 L_2^2}{3} + J_{B2} & 0 \\ 0 & 0 & \frac{m_3 L_3^2}{3} + J_{B3} \end{bmatrix} \in R^{3\times 3},$$

$$M_{24} = \begin{bmatrix} M_{24}^1 & 0 & 0 \\ 0 & M_{24}^2 & 0 \\ 0 & 0 & M_{24}^3 \end{bmatrix} \in R^{3\times 3r},$$

$$M_{24}^i = \begin{bmatrix} \int_0^{L_i} \rho_{Ai} x Y_{i1} dx + J_{Bi} Y'_{i1}(0) & \cdots & \int_0^{L_i} \rho_{Ai} x Y_{ir} dx + J_{Bi} Y'_{ir}(0) \end{bmatrix} \in R^{1\times r},$$

$$M_{44} = \begin{bmatrix} M_{44}^1 & 0 & 0 \\ 0 & M_{44}^2 & 0 \\ 0 & 0 & M_{44}^3 \end{bmatrix} \in R^{3r\times 3r},$$

$$M_{44}^i = \begin{bmatrix} \int_0^{L_i} \rho_{Ai} Y_{i1}^2 dx + J_{Bi} Y_{i1}'^2(0) & \cdots & 0 \\ \vdots & \cdots & \vdots \\ 0 & \cdots & \int_0^{L_i} \rho_{Ai} Y_{ir}^2 dx + J_{Bi} Y_{ir}'^2(0) \end{bmatrix} \in R^{r\times r},$$

https://doi.org/10.1017/S026357471400023X Published online by Cambridge University Press

$$N_1 = \begin{bmatrix} -\frac{1}{2}m_1L_1C_1\dot{\beta}_1^2 - S_1\dot{\beta}_1^2\sum_{j=1}^{r}\int_0^{L_1}\rho_{A1}Y_{1j}q_{1j}dx - 2C_1\dot{\beta}_1\sum_{j=1}^{r}\int_0^{L_1}\rho_{A1}Y_{1j}\dot{q}_{1j}dx \\ -\frac{1}{2}m_2L_2C_2\dot{\beta}_2^2 - S_2\dot{\beta}_2^2\sum_{j=1}^{r}\int_0^{L_2}\rho_{A2}Y_{2j}q_{2j}dx - 2C_2\dot{\beta}_2\sum_{j=1}^{r}\int_0^{L_2}\rho_{A2}Y_{2j}\dot{q}_{2j}dx \\ -\frac{1}{2}m_3L_3C_3\dot{\beta}_3^2 - S_3\dot{\beta}_3^2\sum_{j=1}^{r}\int_0^{L_3}\rho_{A3}Y_{3j}q_{3j}dx - 2C_3\dot{\beta}_3\sum_{j=1}^{r}\int_0^{L_3}\rho_{A3}Y_{3j}\dot{q}_{3j}dx \end{bmatrix} \in R^{3\times 1},$$

$$N_4 = \begin{bmatrix} N_4^1 \\ N_4^2 \\ N_4^3 \end{bmatrix} \in R^{3r\times 1} \quad , \quad N_4^i = \begin{bmatrix} -\dot{\beta}_i^2 q_{i1}\int_0^{L_i}\rho_{Ai}Y_{i1}^2dx \\ \vdots \\ -\dot{\beta}_i^2 q_{ir}\int_0^{L_i}\rho_{Ai}Y_{ir}^2dx \end{bmatrix} \in R^{r\times 1},$$

$$K_f = \begin{bmatrix} K_f^1 + K_p^1 & 0 & 0 \\ 0 & K_f^2 + K_p^2 & 0 \\ 0 & 0 & K_f^3 + K_p^3 \end{bmatrix} \in R^{3r\times 3r},$$

$$K_f^i = \begin{bmatrix} EI\int_0^{L_i}Y''^2_{i1}dx & \cdots & 0 \\ \vdots & \cdots & \vdots \\ 0 & \cdots & EI\int_0^{L_i}Y''^2_{ir}dx \end{bmatrix} \in R^{r\times r},$$

$$K_p^i = \begin{bmatrix} k_p^{i1} & \cdots & 0 \\ \vdots & \cdots & \vdots \\ 0 & \cdots & k_p^{ir} \end{bmatrix} \in R^{r\times r},$$

$$k_p^{ir} = (m_{si}\ddot{\rho}_i - F_{ai})C_i\int_0^{L_i}Y'^2_{ir}dx + \rho_{Ai}\ddot{\rho}_iC_i\int_0^{L_i}xY'^2_{ir}dx - \frac{1}{2}\rho_{Ai}\dot{\beta}_i^2\int_0^{L_i}x^2Y'^2_{ir}dx,$$

$$M_{\rho 1} = \begin{bmatrix} C_1 & S_1 \\ 0 & 0 \\ 0 & 0 \end{bmatrix}, \quad M_{\rho 2} = \begin{bmatrix} 0 & 0 \\ C_2 & S_2 \\ 0 & 0 \end{bmatrix}, \quad M_{\rho 3} = \begin{bmatrix} 0 & 0 \\ 0 & 0 \\ C_3 & S_3 \end{bmatrix} \in R^{3\times 2},$$

$$J_{f\rho} = \begin{bmatrix} M_{\rho 1} & M_{\rho 2} & M_{\rho 3} \end{bmatrix},$$

$$M_{\beta 1} = \begin{bmatrix} -\sum_{j=1}^{r}Y_{1r}(L_1)q_{1r} & L_1 \\ 0 & 0 \\ 0 & 0 \end{bmatrix}, \quad M_{\beta 2} = \begin{bmatrix} 0 & 0 \\ -\sum_{j=1}^{r}Y_{2r}(L_2)q_{2r} & L_2 \\ 0 & 0 \end{bmatrix},$$

$$M_{\beta 3} = \begin{bmatrix} 0 & 0 \\ 0 & 0 \\ -\sum_{j=1}^{r}Y_{3r}(L_3)q_{3r} & L_3 \end{bmatrix} \in R^{3\times 2},$$

$$J_{f\beta} = \begin{bmatrix} M_{\beta 1} & M_{\beta 2} & M_{\beta 3} \end{bmatrix},$$

$$M_{W1} = \begin{bmatrix} \int_0^{L_i}Y'^2_{11}q_{11}dx & Y_{11}(L_1) \\ \vdots & \vdots \\ \int_0^{L_i}Y'^2_{1r}q_{1r}dx & Y_{1r}(L_1) \\ \bar{0}^{2r\times 2} \end{bmatrix}, \quad M_{W2} = \begin{bmatrix} \bar{0}^{r\times 2} \\ \int_0^{L_i}Y'^2_{21}q_{21}dx & Y_{21}(L_2) \\ \vdots & \vdots \\ \int_0^{L_i}Y'^2_{2r}q_{2r}dx & Y_{2r}(L_2) \\ \bar{0}^{r\times 2} \end{bmatrix},$$

https://doi.org/10.1017/S026357471400023X Published online by Cambridge University Press

$$M_{W3} = \begin{bmatrix} \bar{0}^{2r\times 2} \\ \int_0^{L_i} Y'^2_{31} q_{31} dx & Y_{31}(L_3) \\ \vdots & \vdots \\ \int_0^{L_i} Y'^2_{3r} q_{3r} dx & Y_{3r}(L_3) \end{bmatrix} \in R^{3r\times 2},$$

$$J_{fw} = \begin{bmatrix} M_{w1} & M_{w2} & M_{w3} \end{bmatrix},$$

$$J_{PW} = -\begin{bmatrix} \frac{Y_{11}(L)\dot{\beta}_1 L}{a_1\cdot b_1} & \cdots & \frac{Y_{1r}(L)\dot{\beta}_1 L}{a_1\cdot b_1} & 0 & \cdots & 0 & 0 & \cdots & 0 \\ 0 & \cdots & 0 & \frac{Y_{21}(L)\dot{\beta}_2 L}{a_2\cdot b_2} & \cdots & \frac{Y_{2r}(L)\dot{\beta}_2 L}{a_2\cdot b_2} & 0 & \cdots & 0 \\ 0 & \cdots & 0 & 0 & \cdots & 0 & \frac{Y_{31}(L)\dot{\beta}_3 L}{a_3\cdot b_3} & \cdots & \frac{Y_{3r}(L)\dot{\beta}_3 L}{a_3\cdot b_3} \end{bmatrix} \in R^{3\times 3r},$$

$$J_{\beta W} = -\begin{bmatrix} \frac{Y_{11}(L)}{L} & \cdots & \frac{Y_{1r}(L)}{L} & 0 & \cdots & 0 & 0 & \cdots & 0 \\ 0 & \cdots & 0 & \frac{Y_{21}(L)}{L} & \cdots & \frac{Y_{2r}(L)}{L} & 0 & \cdots & 0 \\ 0 & \cdots & 0 & 0 & \cdots & 0 & \frac{Y_{31}(L)}{L} & \cdots & \frac{Y_{3r}(L)}{L} \end{bmatrix} \in R^{3\times 3r},$$

$$M_P = M_{33} = \begin{bmatrix} m_P & 0 & 0 \\ 0 & m_P & 0 \\ 0 & 0 & J_{\phi_p} \end{bmatrix},$$

$$M_{Pi} = \begin{bmatrix} -\cos\beta_i & \sin\beta_i \\ -\sin\beta_i & -\cos\beta_i \\ -r\cos(\beta_i-\theta_i) & -r\sin(\beta_i-\theta_i) \end{bmatrix},$$

$$J_{fP} = \begin{bmatrix} M_{P1} & M_{P2} & M_{P3} \end{bmatrix}$$

$$F_f = -\begin{bmatrix} \operatorname{sign}(\dot{x}_p)\left|\cos(\arctan(\frac{\dot{y}_p}{\dot{x}_p}))\right| & 0 & 0 \\ 0 & \operatorname{sign}(\dot{y}_p)\left|\cos(\arctan(\frac{\dot{y}_p}{\dot{x}_p}))\right| & 0 \\ 0 & 0 & \operatorname{sign}(\dot{\varphi}_p) \end{bmatrix} \begin{pmatrix} m_p g u \\ m_p g u \\ \frac{2}{3} m_p g u R_p \end{pmatrix},$$

$$\theta_1 = \varphi_p, \quad \theta_2 = \frac{\pi}{3} - \varphi_p, \quad \theta_3 = \frac{\pi}{3} + \varphi_p,$$

$$S_i = \sin(\alpha_i - \beta_i), \quad C_i = \cos(\alpha_i - \beta_i),$$

$$a_i = (\cos\alpha_i \quad \sin\alpha_i), b_i = (L\cos\beta_i \quad L\sin\beta_i).$$

https://doi.org/10.1017/S026357471400023X Published online by Cambridge University Press